International Journal of Greenhouse Gas Control 109 (2021) 103352

Contents lists available at ScienceDirect

International Journal of Greenhouse Gas Control

journal homepage: www.elsevier.com/locate/ijggc

Impact of CO_2 leakage from sub-seabed carbon dioxide storage on sediment and porewater geochemistry

Anna Lichtschlag [a,*], Matthias Haeckel [b], David Olierook [c], Kate Peel [a], Anita Flohr [a,c], Christopher R. Pearce [a], Chiara Marieni [d], Rachael H. James [c], Douglas P. Connelly [a]

[a] National Oceanography Centre, European Way, Southampton SO14 3ZH, United Kingdom
[b] GEOMAR Helmholtz Centre for Ocean Research Kiel, Wischhofstr. 1-3, 24148 Kiel, Germany
[c] School of Ocean and Earth Science, National Oceanography Centre, University of Southampton Waterfront Campus, European Way, Southampton SO14 3ZH, United Kingdom
[d] Géosciences Environnement Toulouse, CNRS, 14 Avenue Edouard Belin, 31400 Toulouse, France

ARTICLE INFO

Keywords:
Sediment
CO_2 storage
CO_2 leakage
CO_2-sediment interaction
Geochemistry
Central North Sea
Metal mobilization
Environmental impact

ABSTRACT

Sub-seabed geological CO_2 storage is discussed as a climate mitigation strategy, but the impact of any leakage of stored CO_2 into the marine environment is not well known. In this study, leakage from a CO_2 storage reservoir through near-surface sediments was mimicked for low leakage rates in the North Sea. Field data were combined with laboratory experiments and transport-reaction modelling to estimate CO_2 and mineral dissolution rates, and to assess the mobilization of metals in contact with CO_2-rich fluids and their potential impact on the environment. We found that carbonate and silicate minerals reacted quickly with the dissolved CO_2, increasing porewater alkalinity and neutralizing about 5% of the injected CO_2. The release of Ca, Sr, Ba and Mn was mainly controlled by carbonate dissolution, while Fe, Li, B, Mg, and Si were released from silicate minerals, mainly from deeper sediment layers. No toxic metals were released from the sediments and overall the injected CO_2 was only detected up to 1 m away from seabed CO_2 bubble streams. Our results suggest that low leakage rates of CO_2 over short timescales have minimal impact on the benthic environment. However, porewater composition and temperature are effective indicators for leakage detection, even at low CO_2 leakage rates.

1. Introduction

The rapid increase of atmospheric CO_2 since the start of the industrial revolution has led to global warming, ocean acidification and expanding oxygen minimum zones that are impacting global biodiversity and ecosystem functioning (e.g., Gattuso et al., 2015; Nagelkerken and Connell, 2015). Carbon dioxide capture and storage (CCS) in deep geological reservoirs is seen as a potential mitigation strategy to reduce anthropogenic CO_2 emissions to the atmosphere and keep global warming below the +2 °C target (IEA, 2015). In Europe ample geological storage capacity is located offshore in the North Sea (Vangkilke--Pederson, 2009) in saline aquifers and depleted oil and gas reservoirs (Energy, 2016; Vangkilke-Pederson, 2009). Although the accidental leakage of CO_2 from a sub-seabed storage reservoir is regarded as unlikely (IPCC, 2005), the effects of potential leakage through wells, faults and fractures on the marine environment needs to be assessed in terms of ecosystem response, other consequences for the marine environment, and to identify geochemical parameters that should be monitored as indicators for a leakage from a CO_2 reservoir.

While the distribution and extent of pH plumes in the water column has been modelled for different CO_2 leakage scenarios (Blackford et al., 2020), very little is known about the fluid flow patterns and the effects of sudden high CO_2 concentrations in near-surface sediments. These near-surface sediments play a crucial role for the state and health of the marine environment as they convert, store and release chemical compounds. For example, the majority of nutrient regeneration occurs via remineralization of organic matter in near-surface sediments (Arndt et al., 2013; Middelburg, 2011). One key concern is that leakage of CO_2-rich fluids could result in changes of environmental conditions in the sediment, and hence could lead to disruption of important benthic processes such as carbon degradation (Rastelli et al., 2016). Leakage of CO_2 from offshore CCS reservoirs might reduce biodiversity and might also disrupt important ecological functions, with the impacts on individual biological species differing across different taxonomic groups

* Corresponding author.
E-mail address: a.lichtschlag@noc.ac.uk (A. Lichtschlag).

https://doi.org/10.1016/j.ijggc.2021.103352
Received 23 December 2020; Received in revised form 8 April 2021; Accepted 26 April 2021
Available online 26 June 2021

(Kim et al., 2016). Shallow-marine CO_2-rich seeps are often used as natural analogues to understand ecosystem responses to ocean acidification and CCS leakage (Aiuppa et al., 2021). Studies have shown that high CO_2 concentrations can stimulate seagrass growth (Hall-Spencer et al., 2008), reduce coral diversity (Fabricius et al., 2011), plankton density and diversity (Smith et al., 2016) and change bivalve population structures (Martins et al., 2021). Laboratory experiments on sediment-CO_2 reactions have demonstrated mineral dissolution and metal release from aquifer and near-surface sediments due to desorption and pH decrease, with release of potentially harmful substances, such as toxic metals, into the benthic environment at low pH (Ardelan et al., 2009; Kirsch et al., 2014; Ostertag-Henning et al., 2014; Payán et al., 2012; Wunsch et al., 2014).

Most of the knowledge about the geochemical changes of sediments in contact with high levels of CO_2 comes from laboratory experiments conducted under 'ideal' conditions. Near-shore, shallow-water in-situ CO_2 release experiments have shown that metals will also be released into porewaters under more realistic CO_2 leakage conditions (Lichtschlag et al., 2015), but the processes are much more complex than simulations in the laboratory due to tidal influences, specific seabed properties (Blackford et al., 2014) and the complex movement of the CO_2 through the sediments, including lateral migration (Cevatoglu et al., 2015). However, the extent to which leaking CO_2-rich fluids will react under realistic conditions (e.g., with Central North Sea sediments and at a representative water depth), and the extent to which biogeochemical cycles within the sediment will be disrupted, are poorly understood. A better understanding of the reactions of near-surface sediments with leaking CO_2 is needed for the safe implementation of geologic carbon sequestration and CCS risk assessments and legislation. Stoichiometric relationships between specific geochemical compounds have been proposed as geochemical leakage indicators (Dale et al., 2021), but these have not been tested under leakage conditions and other parameters affected by CO_2 leakage remain to be identified.

Here we report results from a real-world in-situ CO_2 release experiment that was conducted in the UK sector of the North Sea close to the Goldeneye platform, above a depleted reservoir that is considered suitable for CO_2 storage (Cotton et al., 2017; Dean and Tucker, 2017). The experiment mimicked CO_2 leakage into near-surface marine sediments at leakage rates similar to those observed from abandoned wells (Vielstädte et al., 2015). Observations from the in-situ CO_2 release experiment are considered together with transport-reaction modelling and laboratory batch experiments to identify the geochemical components that are mobilized in the event of a CO_2 leakage into sediments, to understand the effect of the fluid movement through sediments and to determine which indicators can be used for CO_2 leakage monitoring. The main aims of this work were to determine the impact of leakage of CO_2 on sediment geochemistry and the benthic environment; to determine how much of the injected CO_2 is neutralized by geochemical reactions within the sediments; and to identify indicator species that can be used as proxies and tracers for CO_2 leakage.

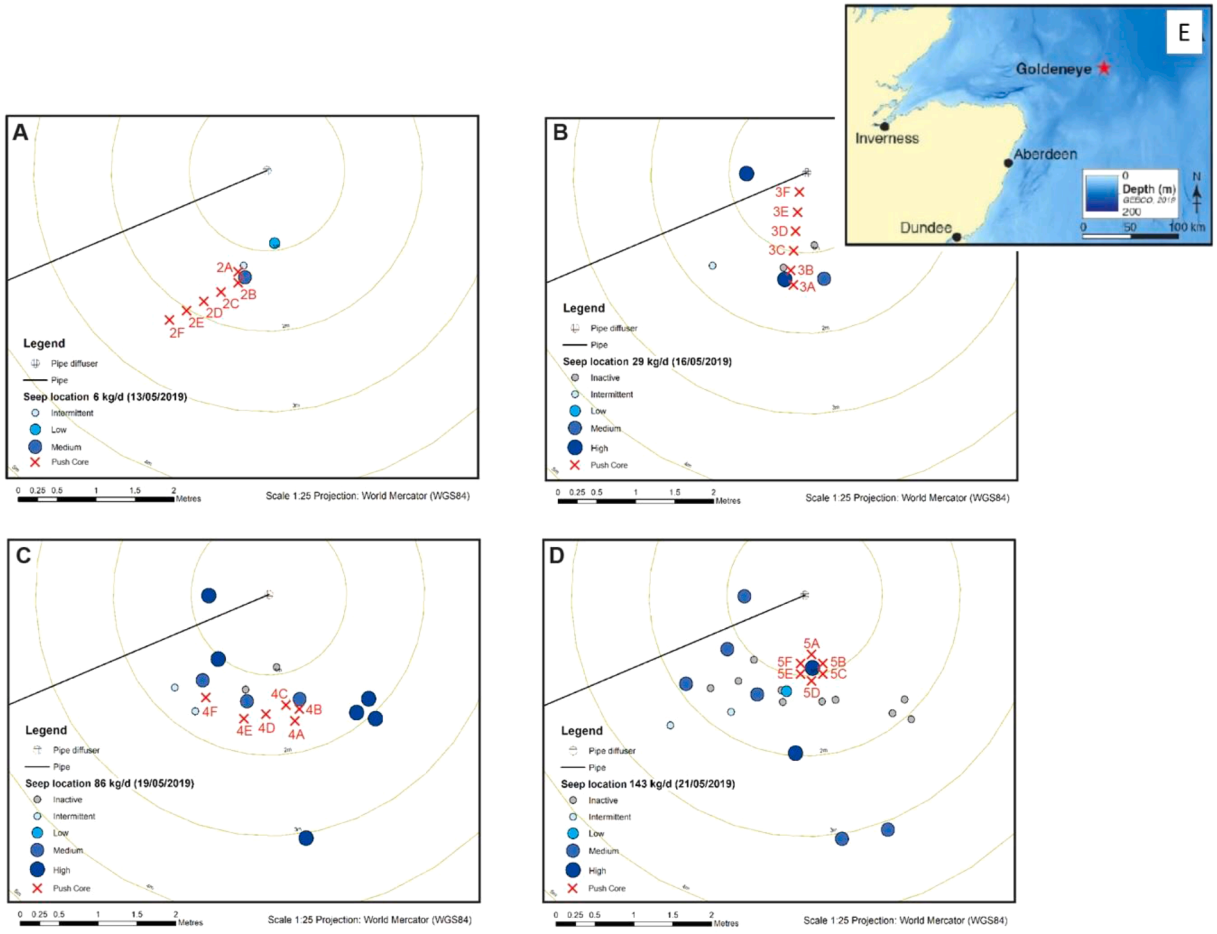

Fig. 1. Map of the area and the locations of the sampled push cores (red crosses) relative to each other and to bubble release sites (blue filled circles), plotted to scale (bubble release map changed after de Beer et al. (2021). A-D show the locations of bubble release sites changing with different flow rates (note that for the 14 kg d^{-1} release rate no map is available; instead the 29 kg d^{-1} release rate map from the same day is displayed; no bubble release was observed post-CO_2 injection; E shows the location of the experiment site close to the Goldeneye platform (red star) in the North Sea.

2. Methods

2.1. Experimental setups

2.1.1. In-situ release experiment

To test the effects of potential CO_2 leakage from CCS storage reservoirs on the geochemistry of near-surface sediments, solid phase and porewater sampling and analyses were done as part of the 'Strategies for Environmental Monitoring of Marine Carbon Capture and Storage' (STEMM-CCS) release experiment in 2019 (e.g., Flohr et al., 2021b). The experimental area was located ~800 m southeast of the Goldeneye platform in the Central North Sea (UK Sector, 120 m water depth, Fig. 1). During the release experiment, gaseous CO_2 was injected through a pipe 3 m below the seafloor and entered the sediment through a 40 cm long diffuser. Over the course of 11 days, CO_2 was injected into the sediment at different flow rates that were increased in steps: day 1: 6 kg d^{-1}; day 4: 14 kg d^{-1}; day 5: 29 kg d^{-1}, day 7: kg d^{-1}; day 9: 143 kg d^{-1}. In total, 675 kg of CO_2 were injected. Less than 30 min after the injection started, gas bubbles were observed leaving the sediment surface; throughout the experiment up to 15 individual gas bubble streams (henceforth called bubble sites) were observed (Flohr et al., 2021a; Fig. 1). A chimney-type structure approximately 15 m in diameter and located at 200 - 300 cm sediment depth was observed (using seismic techniques) to have emerged after the gas injection started (Roche et al., 2021).

During most of the CO_2 injection steps, as well as prior and post CO_2 injection, approximately 25 cm long push cores were collected with the remotely operated vehicle (ROV) ISIS during the RRS *James Cook* expedition JC180. A set of 6 push cores were collected at various distances from the bubble sites during separate ROV dives (Fig. 1); one core, taken close to a bubble site, was dedicated to solid phase analyses and the remaining cores were used for porewater analyses. The distance from the bubble site was determined by visual inspection during the ROV dives. The sediment cores for solid phase analyses were subsampled in 1 cm intervals in the upper 10 cm and in 2 cm intervals below. Subsamples of the solid phase were either frozen at −20 °C for organic and inorganic carbon analyses and carbon isotopic ratio analyses or stored at 4 °C for porosity, XRF and XRD analyses. The remaining cores were handled in a temperature-controlled room set to 9 °C in an anaerobic chamber filled with N_2 to prevent oxidation of redox-sensitive porewater species. Inside the anaerobic chamber the sediments were sectioned horizontally at the same intervals as the solid phases, and the sediments were placed in 50 mL centrifuge vials with a hole in the lid. To collect porewaters, a Rhizon sampler (Rhizosphere Research Products, Wageningen) was introduced through the hole, connected to a syringe and a small underpressure was applied. The first 0.5 mL of porewater was discarded and the remaining porewater was split into aliquots: 1 mL to a plastic pot for on board total alkalinity (TA) analysis; 2 mL in an acid cleaned plastic bottle for cation analysis, acidified with 5 μL thermally distilled concentrated HNO_3; 1 mL into a plastic vial for nutrient analysis stored frozen at −20 °C and 1 mL stored at 4 °C for analysis of SO_4. Prior to the CO_2 injection, gravity cores and multi cores were collected during research expedition POS527 to determine the geochemical and physical properties of the upper 430 cm of the sediment (Table 1). Porewater was extracted from the gravity core sediments with Rhizons through holes drilled in the core liners, sediment was subsampled with cut-off syringes every 20 cm, and similar aliquots were taken as described above.

2.1.2. Laboratory experiment

Reaction experiments between sediments from the Central North Sea and CO_2 were undertaken in the laboratory following the procedure described in Marieni et al. (2020). For this, sediments were collected from close to the experimental area in 2017 during POS518 with a gravity corer (14–2 GC 3) and a multi corer (MUC-4 1B; Table 1) and sediment subsamples were frozen immediately after sampling at −20 °C to prevent oxidation of reduced species. Four intervals, i.e., 0–1 cm, 41–45 cm, 228–232 cm and 398–402 cm below seafloor, were chosen as they had layers with distinctively different geochemical and geophysical properties (Fig. 2). Approximately 20 g of sediment from each interval was exposed to 1 L of 1-bar CO_2 saturated artificial seawater (Tropic Marine Pro-Reef Salt) for 24 days. Each day a sample (approximately 2 mL) of the overlying water was taken with a syringe and the total alkalinity (TA) and cation concentrations were measured as described below. The pH in the water was measured with a Mettler Toledo SevenMultiTM pH metre equipped with an InLab® Micro Pro-ISM glass pH electrode. A control experiment with CO_2-saturated seawater, but without sediment, was conducted simultaneously. The grain size of the sediment samples was determined before and after the experiment as described below.

2.2. Geochemical analyses

2.2.1. Sediment analyses

The chemostratigraphy of the upper 430 cm of GC06 sediments collected during POS527, was determined with the Cox Analytical Systems ITRAX core scanner (Croudace et al., 2006) at the British Ocean Sediment Core Research Facility (BOSCORF). Core scanning was performed on the split core surfaces and X-ray fluorescence (XRF) data was acquired using a 3 kW molybdenum (Mo) X-ray tube operated with a voltage of 30 kV, a current of 30 mA, a count time of 15 s and an analysis resolution of 1 mm. Element counts (Ca, Sr, Si, Fe, Mn, K and Br) were normalized to kilo-counts per second (kcps) and a running average of 5 mm was applied to the results. The major and minor element composition of the sediments was determined by X-ray fluorescence (XRF, Philips MagiX-pro Wavelength dispersive X-ray fluorescence spectrometer, fitted with a 4 kW Rh end-window X-ray tube) on fused glass beads for the major elements and on pellets pressed into bricks for the minor

Table 1
Details of sediment cores taken during POS518, POS527 and JC180 (i.e., pre-, during and post-CO_2 release). During JC180 (i.e., the CO_2 release experiment) core 'A' was taken closest (i.e., < 2–4 cm) to the different bubble sites, except 4A, which was taken 12 cm away from a bubble site; cores 'B-F' were taken in different distances from the bubble sites as shown in Fig. 3.

Core ID	Expedition	Sampling device	Gas flow (kg d^{-1})	Day of release	Latitude	Longitude
Pre-release						
MUC-4 1B	POS518	multi corer	0	<0	57° 59.690′	00° 22.330′
14–2 GC 3	POS518	gravity corer	0	<0	57° 59.648′	00° 22.247′
GC 06	POS527	gravity corer	0	<0	57° 59.734′	00° 22.383′
1 A-D	JC180	push core	0	−4	57° 59.672′	00° 22.479′
During release						
2 A-F	JC180	push core	6	1	57° 59.680′	00° 22.447′
3 A-F	JC180	push core	14	4	57° 59.670′	00° 22.486′
4 A-F	JC180	push core	86	7	57° 59.676′	00° 22.459′
5 A-F	JC180	push core	143	9	57° 59.680′	00° 22.434′
Post-release						
6 A-D	JC180	push core	0	+5 (15)	57° 59.650′	00° 22.462′

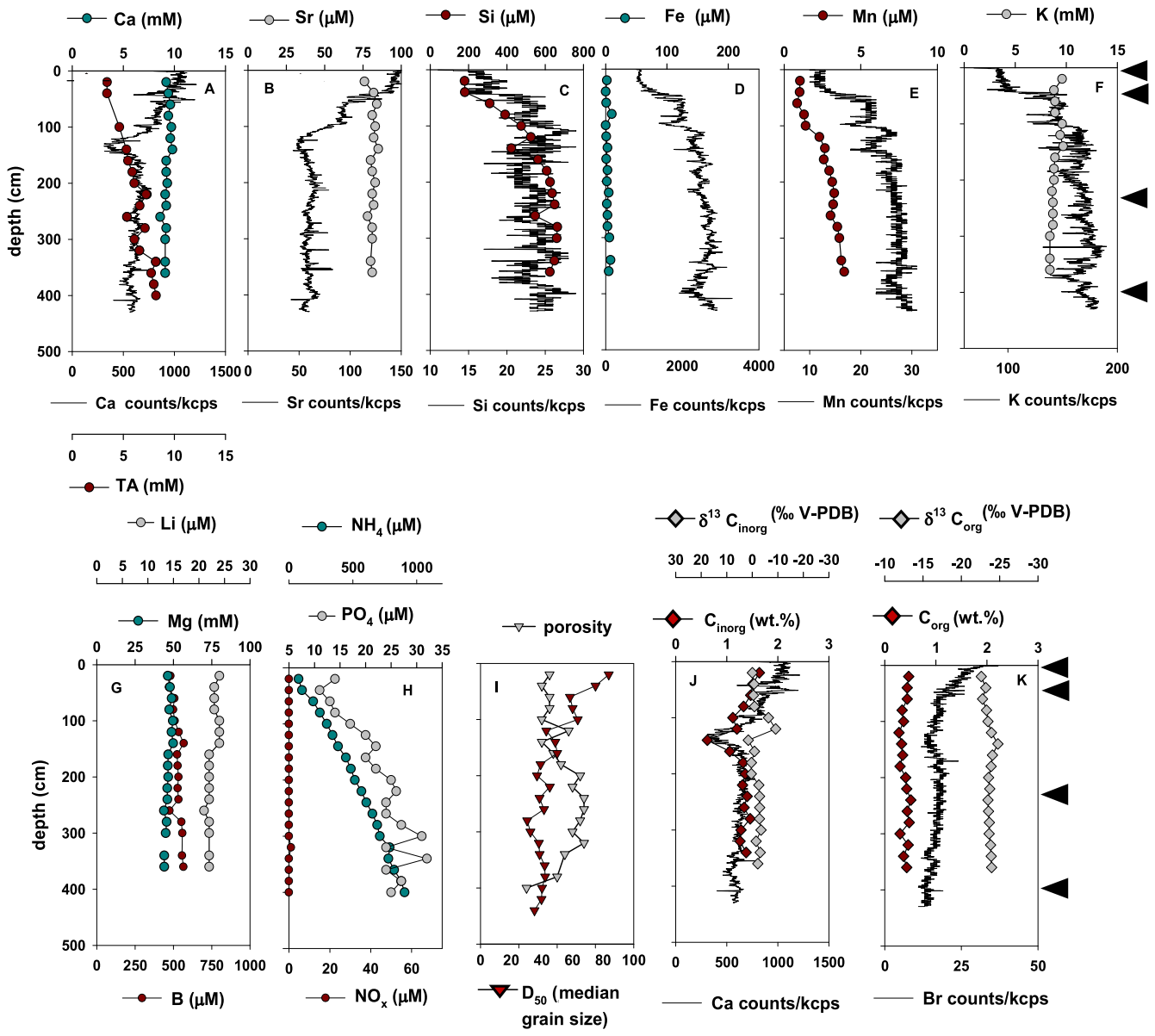

Fig. 2. Geochemical porewater (filled circles), solid phase (filled squares, black lines for ITRAX chemostratigraphy) and geophysical properties (filled triangles) of core GC06 collected during POS527 about 150 m NE of the CO_2 release experiment site before the start of the CO_2 injection into the sediments. The sample intervals that were used in the laboratory experiment and for the sequential extractions are indicated by the black arrows. These samples were collected during POS518, and the downcore variations of the geochemical parameters of the cores they came from are similar to those shown here (Dale et al., 2021).

elements. Mineralogy of the sediments was determined on selected samples by X-ray diffraction. X-ray diffraction patterns were recorded on a Philips X'Pert Pro-diffractometer, using CuKα radiation (35 kV, 40 mA) at angles from 2 to 76° with a step size of 0.02° and acquisition time of 1.2 s per step. Mineral phases were qualitatively identified with the Philips XPert software, which is based on the PDF database from the JCPDS (Joint Committee on Powder Diffraction Standards). Organic and inorganic carbon composition and stable carbon isotope ratios ($\delta^{13}C$) were determined with a Flash 2000 Elemental Analyser (EA) coupled to a Delta V Advantage Isotope ratio mass spectrometer (IRMS) via a ConFlo IV Continuous Flow interface (both Thermo Fisher Scientific). For measurements of organic carbon content (C_{org}) and its isotopic composition, the inorganic carbon was removed with 3 M HCl. The inorganic carbon content (C_{inorg}) was calculated by subtracting the C_{org} from the total carbon content (C_{tot}) and the isotopic ratio of C_{inorg} was calculated from the contents and isotopic ratio of the different carbon fractions. All isotope data are reported in the conventional delta notation relative to the Vienna Pee Dee Belemnite (V-PDB) standard. Analytical precision for C_{org} and C_{tot} was 0.17 wt.%, and for $\delta^{13}C$ it was ±0.58 ‰ V-PDB. The grain size of the sediments was measured as the average of ten measurements (standard deviation < 3%) with a Malvern Mastersize 3000 after shaking the samples overnight in RO water to disaggregate them. The porosity of the sediments was determined by difference between the wet sediment and sediment dried in the oven at 60 °C for a minimum of 72 h, assuming a sediment density of 2.6 g cm^{-3}.

2.2.2. *Porewater analyses*

Total alkalinity (TA) measurements were conducted by titrating against 0.0004 M HCL (for low TA samples) or 0.002 M HCl (for high TA samples) using a mixture of methyl red and methylene blue as indicator

and removing CO_2 by constant bubbling with N_2. Analyses were calibrated against the International Association for the Physical Sciences of the Oceans (IAPSO) seawater standard measured in triplicate at the beginning of each analytical session and monitored with Dickson CRM 164 (accuracy and precision better than 3%).

Porewater concentrations of cations (Al, B, Ca, Cu, Fe, K, Li, Mn, Ni, Mg, Pb, Rb, Si, and Sr) were determined by inductively coupled plasma optical emission spectrometry (ICP-OES, Thermo Scientific Icap 6500 duo) after diluting samples by a factor of 50 with 3% thermally distilled HNO_3. Measured concentrations of certified reference material for metals (CRM -SW, High-Purity Standards - seawater) were mainly within ± 5% (Ca, Mg, Li, Sr, Na, B, Si) of the certified values. Al, Cu, Ni and Pb were below detection limit (0.02 µM, 0.02 µM, 0.013 µM, and 0.01 µM, respectively). Total dissolved phosphate (PO_4), NOx (= NO_2 plus NO_3) and ammonium (NH_4) concentrations were measured with a QuAAtro nutrient analyser after diluting the samples five times with MilliQ water. Detection limits were 0.014 µM (PO_4), 0.022 µM (NO_X) and 0.735 µM (NH_4). Sulphate concentrations were measured with a Dionex Aquion (Thermo Fisher Scientific) ion chromatograph and precision and accuracy was better than 2%.

2.2.3. Sequential extractions

To assess the potential mineralogical source of elements released into the porewater (carbonate-bound, easily-reducible oxides, reducible oxides or magnetite) and assess if different elements can be leached from different layers of the sediment, sequential extractions were performed after the method described in Poulton and Canfield (2005). In brief, 0.1–0.2 g of frozen sediment was leached in 10 mL of: 1) acetic acid buffered to a pH of 4.5 for 4.5 h (to extract carbonate-associated phases); 2) 1 M hydroxylamine hydrochloride solution in 25% v/v acetic acid for 48 h (to extract metals associated with easily reducible Fe and Mn oxides; 3) 50 g L^{-1} sodium dithionite with 0.35 M acetic acid buffered to pH 4.8 for 2 h (to extract metals associated with reducible Fe and Mn oxides, such as goethite, akaganeite and haematite); and 4) 0.2 M ammonium oxalate buffered to pH 3.2 with 0.17 M oxalic acid for 6 h (to extract metals associated with magnetite). After each step, sediments were centrifuged and the chemical composition of the supernatants were measured with ICP-OES as described above.

2.3. Modelling

In order to determine rates of CO_2 dissolution and subsequent carbonate and silicate mineral dissolution induced by the injection of gaseous CO_2, we applied a numerical transport-reaction model (Haeckel and Wallmann, 2008; Zander et al., 2020) using the parameters and boundary conditions presented in Tables 2 and 3. The model considers the solute variables TA, total dissolved inorganic carbon (DIC, treating the carbon isotopes $^{12}C_{DIC}$ and $^{13}C_{DIC}$ separately to account for the carbon isotope contributions from CO_2 and $CaCO_3$ dissolution; $^{13}C_{DIC}$, DIC data presented in Flohr et al., 2021a), Ca, Mg, Sr, Li, B, Si as well as carbonate and silicate mineral phases and amorphous silica. According to Berner (1980) early diagenesis of solutes and solids is governed by the partial differential equations:

$$\frac{\partial \Phi C}{\partial t} = \frac{\partial}{\partial x}\left(\Phi D_s \frac{\partial C}{\partial x} + u\Phi C\right) + \Phi\,\alpha(C_0 - C) + \Phi\sum_j R_j$$

$$\frac{\partial (1-\Phi) C}{\partial t} = \frac{\partial}{\partial x}\left((1-\Phi) D_B \frac{\partial C}{\partial x} + w(1-\Phi)C\right) + (1-\Phi)\sum_j R_j$$

where Φ is the porosity, C is the concentration of a solute or solid component, t is time, $D_s = \frac{D_0}{1-2\ln\Phi}$ is the molecular diffusion coefficient of the solute corrected for sediment tortuosity (Boudreau, 1997), α is the bioirrigation coefficient, C_0 is the solute concentration in the bottom water, D_B is the bioturbation coefficient, u is the vertical advection velocity of the porewater, w is the vertical sediment burial velocity, and $\sum R_j$ represents the biogeochemical reaction rates relevant to the species under consideration. For the simulated time scale of a few weeks, the transport term of solids can be neglected by setting D_B and w to zero, as can solute bioirrigation (i.e., α is also set to zero). Biological mixing activity by benthic fauna is also expected to be inhibited as a result of the low pH during CO_2 leakage.

The overpressure created by the CO_2 injection induces upward-directed porewater flow that can be estimated using Darcy's law:

$$u(x,t) = -\frac{\Phi_0}{\Phi(x,t)}\,\frac{\kappa}{\mu}\,\frac{dp}{dx}$$

where κ is the effective permeability of the overburden sediments, µ is the dynamic viscosity of the porewater, and dp is the overpressure measured at the back valve with respect to the hydrostatic pressure at the injection point, i.e., about 0.7 bar (Flohr et al., 2021a).

Steady-state compaction of the sediment is prescribed by an exponentially decreasing porosity profile (least-squares fitted to the measured data):

Table 2
Model parameters used in this study.

Parameter	Notation/Unit	Value
Length of model domain	x/cm	300
Bottom water temperature	T_{BW}/°C	[c] 7.75
Hydrostatic Pressure	p/MPa	[c] 1.19
Bottom water salinity	S	[c] 35.5
Porewater density	ρ_w/kg m^{-3}	[a] 1028
Sediment grain density	ρ_s/kg m^{-3}	[a] 2500
Porosity at sediment surface	ϕ_0/m^3 m^{-3}	[b] 0.602 (21)
Porosity at infinite depth	ϕ_∞/m^3 m^{-3}	[b] 0.485 (16)
Exponential coefficient for porosity decrease	β/cm^{-1}	[b] 0.153 (71)
Effective sediment permeability	κ/cm^2	[e] 1.9 10^{13}
Dynamic viscosity of the porewater	µ/Pa s	[a] 0.0015
Solubility of carbon dioxide gas	L_{MB}/mM	[a] 595
Solubility product of calcium carbonate mineral	L_{CaCO3}/mM^2	[e] 1.43
Solubility of Mg-silicate mineral	L_{MgSi}/mM	[e] 200
Solubility of amorphous silica	L_{SiO2}/mM	[e] 0.2
Rate constant for carbon dioxide gas dissolution	k_{CO2}/a^{-1}	[e] 500
Rate constant for carbonate mineral dissolution	k_{CaCO3}/mM a^{-1}	[e] 300
Rate constant for Mg-silicate mineral dissolution	k_{MgSi}/mM a^{-1}	[e] $1 \cdot 10^7$
Rate constant for amorphous silica precipitation	k_{SiO2}/mM a^{-1}	[e] 50
Heat capacity of porewater	c_w/J g^{-1} K^{-1}	[a] 3.98
Heat capacity of sediment grains	c_s/J g^{-1} K^{-1}	[a] 0.86
Thermal conductivity of porewater	λ_w/W m^{-1} K^{-1}	[a] 0.58
Thermal conductivity of sediment grains	λ_s/W m^{-1} K^{-1}	[a] 1.2
Reaction enthalpy of carbon dioxide dissolution	ΔH_{CO2}/kJ mol^{-1}	[d] −20
Reaction enthalpy of calcium carbonate dissolution	ΔH_{CaCO3}/kJ mol^{-1}	[d] −9.6
Reaction enthalpy of Mg-silicate mineral dissolution	ΔH_{MgSi}/kJ mol^{-1}	[d] −108
Reaction enthalpy of amorphous silica precipitation	ΔH_{SiO2}/kJ mol^{-1}	[d] −14
Carbon isotopic signature of carbon dioxide gas	$\delta^{13}C_{CO2}$/‰	[c] +19
Carbon isotopic signature of carbonate minerals	$\delta^{13}C_{CaCO3}$/‰	[c] +0

[a] Values calculated according to algorithms in Kossel et al. (2013) and references therein.

[b] Result of least-squares fitting of porosity equation to data. Variance of fit is 0.00085, χ^2 is 0.0856, and 2-σ standard deviation of fit parameters are given as last digits in brackets.

[c] Observed field data.

[d] Values according to Stumm and Morgan (1996).

[e] Adjusted values for reproducing the observed data.

Table 3
Boundary conditions of the model variables.

Boundary conditions	$x = 0$,t	$x = z$,t
Total alkalinity, TA	2.45 meq L^{-1}	$dC/dx = 0$
Total dissolved inorganic carbon, DIC	2.3 mM	$dC/dx = 0$
Carbon isotopic signature of DIC, $\delta^{13}C_{DIC}$	−2.0 ‰	$dC/dx = 0$
Dissolved calcium, Ca	10.5 mM	$dC/dx = 0$
Dissolved magnesium, Mg	55 mM	$dC/dx = 0$
Dissolved strontium, Sr	87 μM	$dC/dx = 0$
Dissolved lithium, Li	25 μM	$dC/dx = 0$
Dissolved boron, B	0.41 mM	$dC/dx = 0$
Dissolved silica, Si	100 μM	$dC/dx = 0$
Solid carbonate mineral, (Ca,Mg,Sr)CO_3	15 wt%	$dC/dx = 0$
Solid Mg-silicate mineral, (Ca,Mg,Sr)$Al_2Si_2O_8$	10 wt%	$dC/dx = 0$
Solid amorphous silica, SiO_2	0 wt%	$dC/dx = 0$
Temperature, T	7.75 °C	$dT/dx = 0$

Note: $^{12}C_{DIC}$ and $^{13}C_{DIC}$ concentrations are calculated from DIC and $\delta^{13}C_{DIC}$: $^{12}C_{DIC} = \mathrm{DIC}\frac{1}{1+r}$ and $^{13}C_{DIC} = \mathrm{DIC}\frac{r}{1+r}$ with $r = \left(\frac{\delta^{13}C}{1000}+1\right)\left(\frac{^{12}C}{^{13}C}\right)_{VPDB}$. The $^{12}C/^{13}C$ ratio of the Vienna Pee Dee Belemnite (V-PDB) standard is 0.0111802 (Werner and Brand, 2001).

$$\Phi(x,t) = \Phi_\infty + (\Phi_0 - \Phi_\infty)e^{-\beta x}$$

where ϕ_0 is the porosity at the sediment surface ($x = 0$), ϕ_∞ is the porosity at the sediment surface ($x=\infty$), and β is the attenuation coefficient.

The following reactions, R_j, are considered in the transport-reaction model (see Tables 2 and 3 for variable explanations):

a) Carbon dioxide (CO_2) gas dissolution: $R_{CO2} = k_{CO2}(L_{CO2} - CO_2)$,

b) Calcium carbonate ($CaCO_3$) dissolution: $R_{CaCO3} = k_{CaCO3}\left(\frac{Ca^*CO_3}{L_{CaCO3}} - 1\right)$,

c) Magnesium (Mg)-silicate (Si) mineral dissolution (Oelkers, 2001): $R_{MgSi} = k_{MgSi}\sqrt{\frac{L_{MgSi}}{Mg}}a_{H^+}$,

d) Amorphous silica (SiO_2) precipitation: $R_{SiO2} = k_{SiO2}\left(\frac{SiO2}{L_{SiO2}} - 1\right)$.

The stoichiometric factors for the modelled solutes released by carbonate and silicate mineral dissolution are provided in Table 4.

Finally, the temperature, T, of the bulk sediment is considered by an equivalent partial differential equation:

$$\frac{\partial}{\partial t}\left(\left[(\rho_w c_w)^{\Phi}(\rho_s c_s)^{1-\Phi}\right]T\right) = \frac{\partial}{\partial x}\left(\left[\Phi\rho_w\lambda_w + (1-\Phi)\rho_s\lambda_s\right]\frac{\partial T}{\partial x} - u\Phi\rho_w c_w T\right) + \Phi\sum_j R_j\Delta H_j$$

where ρ_i is the density of phase i, c_i its heat capacity, and λ_i its thermal conductivity with i = w and s referring to the porewater and sediment grains, respectively. ΔH_j is the enthalpy of the respective reaction. In the above equation, the bulk heat capacity is calculated as geometric mean and the bulk thermal conductivity as arithmetic mean of the volumetric contributions of the porewater and sediment.

Table 4
Stoichiometric factors for solute release from carbonate and silicate mineral dissolution.

Solute	*Carbonate*	*Silicate*
Total alkalinity, TA	2	2
Total dissolved inorganic carbon, DIC	1	0
Dissolved calcium, Ca	0.9058	0.125
Dissolved magnesium, Mg	0.090	0.875
Dissolved strontium, Sr	0.0035	0.0003
Dissolved lithium, Li	0.0007	0.005
Dissolved boron, B	0.014	0.05
Dissolved silica, Si	0	2

3. Results

3.1. Geochemical characteristics of Central North Sea sediments

The geochemical composition of the sediments and porewaters to a depth of up to 430 cm below seafloor (i.e., covering the CO_2 injection depth) prior to CO_2 injection are shown in Fig. 2. Sediments are composed of a mixture of poorly sorted sandy muds and muddy sands, a porosity of about 50% and finer sediments below 120 cm below seafloor. The sediments are siliciclastic and consist of quartz (50–70 wt.%), plagioclase (9–12 wt.%), orthoclase (3–9 wt.%), calcite (3–9 wt.%), clay minerals (2–29 wt.%) and some dolomite below 200 cm below seafloor (Table 5). The general increase of clay minerals and decrease of quartz and calcite with depth is related to a change from more sandy to more muddy sediments. The mineralogy of the sediments is confirmed by its geochemical composition (Table 6), which is dominated by SiO_2 (60–70 wt.%), with CaO decreasing from 9 to 5 wt.%, Fe_2O_3 increasing from 1 to 5 wt.%, MnO increasing from 0.03 to 0.08 wt.% and Al_2O_3 increasing from 6 to 13 wt.% with depth, due to the higher proportion of clays at depth. The down-core changes in element composition are confirmed by the ITRAX chemostratigraphy, showing a relative decrease in Ca and Sr with depth and an increase in Si, Fe, Mn and K (Fig. 2). Sr and Ca are strongly positively correlated ($R^2 = 0.99$, Supplement Fig. 3), suggesting that Sr is principally associated with carbonates. This is corroborated by the molar ratio of Sr/Ca of ~0.0035, which is very close to the typical ratio of marine carbonates (Table 4). C_{inorg} decreases from around 2 wt.% at the sediment-water interface (Supplement Fig. 1) to approximately 1.3 wt.% at 400 cm below seafloor (Fig. 2) with $\delta^{13}C_{inorg}$ ranging from −9 to 0 ‰ V-PDB (Fig. 2., Supplement Fig. 1), typical of marine carbonates. Converting the C_{inorg} and the Ca from XRF into wt.% Ca-carbonate and comparing them to the XRD yields similar values, indicating that the majority of Ca in the sediment is associated with carbonate minerals, whereas other Ca-containing minerals (e.g., Ca-rich feldspars) are likely not abundant. The organic carbon content of the sediments is around 0.7 wt.% with a $\delta^{13}C$ value of around −23‰ V-PDB (Fig. 2, Supplement Fig. 1), typical for marine organic carbon. The element distribution in the sediments is consistent with early diagenetic processes, authigenic carbonate formation and ongoing alteration by reverse weathering leading to the formation of authigenic clays (Dale et al., 2021).

The geochemical composition of the porewater in the upper 430 cm of the sediments prior to the CO_2 injection is similar to that reported previously from the area (Dale et al., 2021) with dissolved Ca, Sr, Li, K and Mg concentrations similar to seawater (i.e., 10 mM, 75 μM, 25 μM, 8.5 mM and 50 mM); dissolved iron <1 μM and dissolved Si and Mn increasing with depth to 600 μM and 5 μM, respectively (Fig. 2). Nutrient concentrations are similar to those previously reported from this site (Dale et al., 2021), with NO_x below detection limit, and PO_4 and NH_4 increasing with depth to 30 and 900 μM, respectively. TA values increase to a maximum of 8 mM at 400 cm depth. Higher resolution sampling in the upper 25 cm of the sediment prior to the injection start (Fig. 3) show that concentrations of dissolved Fe, Mn, PO_4 and NO_x are highest close to the sediment surface, indicative of anaerobic carbon degradation (Dale et al., 2021).

3.2. Geochemical changes during the in-situ CO_2 release

Changes in the chemical composition of the porewaters were detected immediately after CO_2 injection started. Initially, shifts (Δ_x, the difference in the concentration of species x in porewater samples before and after the start of CO_2 injection) were of the order ΔTA = 16.5 mM and ΔCa = 5 mM, but were mostly restricted to within ~5 cm of the bubble sites (Fig. 3). By day 4 (gas flow rate = 14 kg CO_2 d^{-1}), no further

Table 5
Mineralogical composition (XRD) of sediments collected in the vicinity of the CO_2 release experiment site before the start of the CO_2 injection into the sediments; < d. l. = below detection limit.

	Quartz (wt.%)	Calcite (wt.%)	Plagioclase (wt.%)	Orthoclase (wt.%)	Clays (wt.%) *Muscovite, Biotite, Chlorite, Kaolinite*	Dolomite (wt.%)
0–1 cm	64.4	9.0	11.2	7.7	2.4	< d. l.
9–10 cm	69.0	8.3	10.2	6.9	2.0	< d. l.
18–20 cm	66.5	7.7	11.6	7.6	2.7	< d. l.
20 cm	65.3	8.5	8.7	8.6	1.5	< d. l.
200 cm	49.4	5.8	9.7	6.4	8.5	2.1
300 cm	51.3	6.4	8.7	3.0	28.6	2.0
400 cm	62.5	3.3	10.1	2.9	20.0	1.2

Table 6
Major and minor element composition of selected sediment samples prior to the start of CO_2 injection. LOI = Loss on Ignition.

Major elements	SiO_2 wt.%	TiO_2 wt.%	Al_2O_3 wt.%	Fe_2O_3 wt.%	MnO wt.%	MgO wt.%	CaO wt.%	K_2O wt.%	Na_2O wt.%	P_2O_5 wt.%	LOI wt.%
0–1 cm	66.4	0.4	6.0	1.6	0.03	0.9	9.1	1.9	1.7	0.1	11.9
41–45 cm	69.6	0.3	5.9	1.4	0.03	0.8	8.2	1.9	1.6	0.1	10.2
228–232 cm	60.3	0.6	11.1	4.3	0.06	2.3	6.0	2.9	1.7	0.1	10.7
398–402 cm	60.0	0.7	13.0	5.1	0.08	2.5	5.2	3.3	1.7	0.1	8.3

Minor elements	Ba ppm	Cr ppm	Cu ppm	Mo ppm	Nb ppm	Ni ppm	Pb ppm	Rb ppm	Sr ppm	V ppm	Zn ppm	Zr ppm
0–1 cm	419	51	7	0	6	3	11	52	340	41	32	228
41–45 cm	384	44	6	0	5	1	11	50	311	32	28	244
228–232 cm	422	89	16	1	10	25	16	99	189	110	64	210
398–402 cm	434	90	24	0	13	26	20	120	167	131	77	207

changes in porewater geochemistry were observed, indicating that the distribution of CO_2 in the sub-seabed sediments was restricted to the area in the immediate vicinity of the gas bubble sites. By day 7 (gas flow rate = 86 kg CO_2 d^{-1}), significant changes in porewater chemistry of sediments sampled close to individual bubble streams were observed, with ΔTA = 32 mM and ΔCa = 13 mM. In addition, concentrations of Si (Δ375 μM), Mn (Δ21 μM), NH_4 (Δ143 μM) and PO_4 (Δ33 μM) had all increased and a peak in Fe was measured at the sediment surface (Δ110 μM) (Fig. 3). The largest increases in sediments sampled close to individual bubble streams were found at the highest injection rate (143 kg CO_2 d^{-1}) on day 9 of the experiment, with TA and Ca increasing by 44 mM and 19 mM compared to background concentrations. At this flow rate, increases of Si (Δ590 μM), NH_4 (Δ110 μM) and Mn (Δ13 μM) were measured. Also, a distinct peak of dissolved iron was present (up to 200 μM) at 5 cm below the sediment-seawater interface. Porewater concentrations of TA, Ca and Si were still elevated 5 days after the injection had stopped, though Fe and Mn concentrations had returned to pre-injection values. Interestingly, peaks of up to 75 μM NO_x were measured close to the sediment surface (i.e., 5 times higher than prior the experiment start) at the same depth interval where NH_4 concentrations were decreased.

Other elements that had distribution patterns similar to TA and Ca were Sr (max. Δ82 μM,) B (max. Δ334 μM), Li (max. Δ10 μM) and Rb (max. Δ56μM), but increases were usually not more than 1.5–3 times higher than the initial values. Changes in Mg and SO_4 were within analytical errors of the measurements and concentrations of Al, Cu, Pb and Ni were below detection limit. In the solid phase, grain size, porosity, C_{inorg} and C_{org} in sediments close to the bubble release sites remained constant within the time frame of the experiment (Supplement Fig. 1).

3.3. Batch laboratory experiments

In the laboratory, sediments exposed to CO_2-saturated seawater showed rapid increases in the cation concentrations in the overlying waters, indicating dissolution of minerals (Fig. 4). At the start of the experiment (day 0), the pH of the seawater fell to < 5.2 due to dissolution of CO_2, but pH then increased rapidly to values around 5.8–6 as mineral dissolution started. In the control-experiment, the CO_2-saturated solution had a pH of 5 and a TA of 3.3 mM. Cation release from sediments was highest in the first 4 days of the experiment, but some mineral dissolution continued until the end of the experiment. The release patterns of TA, Ca, Sr and B with time into solution were similar and maximum concentration differences of ΔTA = 12–20 mM, ΔCa = 8–13 mM, ΔSr = 10–30 μM and ΔB = 18–50 μM were measured. For these compounds more cations were released from near-surface sediments than from those below 200 cm depth. A different behaviour was seen for Mn, which was released from all sediments (Δ6–41 μM), but 8 times more from the deeper layers. Fe and Si were only released from the deeper sediment layers and highest concentrations were measured during the first 1–2 days of the exposure of the sediment to CO_2-satured seawater. Afterwards, concentrations of these elements in the solution decreased, indicating re-precipitation. Other elements, such as Mg, Li, Na and K (Na and K data are not shown), did not show consistent changes in solution over the course of the experiment. Concentrations of Cu, Pb and Ni were below the detection limit. Grain size analysis showed that the deeper sediments were much finer grained than the surface sediments and that the particle sizes decreased over the course of the experiment (Fig. 4).

3.4. Sequential extractions

Results of sequential leaching of the sediments are show in Fig. 5. The majority of Ca (>75%) was released from minerals during the first extraction step (carbonate-associated), showing that carbonates are the major source of Ca in the sediments. Sr showed a similar behaviour, confirming that Sr was mostly bound to carbonates. About 25% of the Mg was liberated by the dissolution of the carbonate fraction and leachable Mn was also mainly associated with carbonates, notably in the deeper sediments. 14–33% of the iron was associated with easily

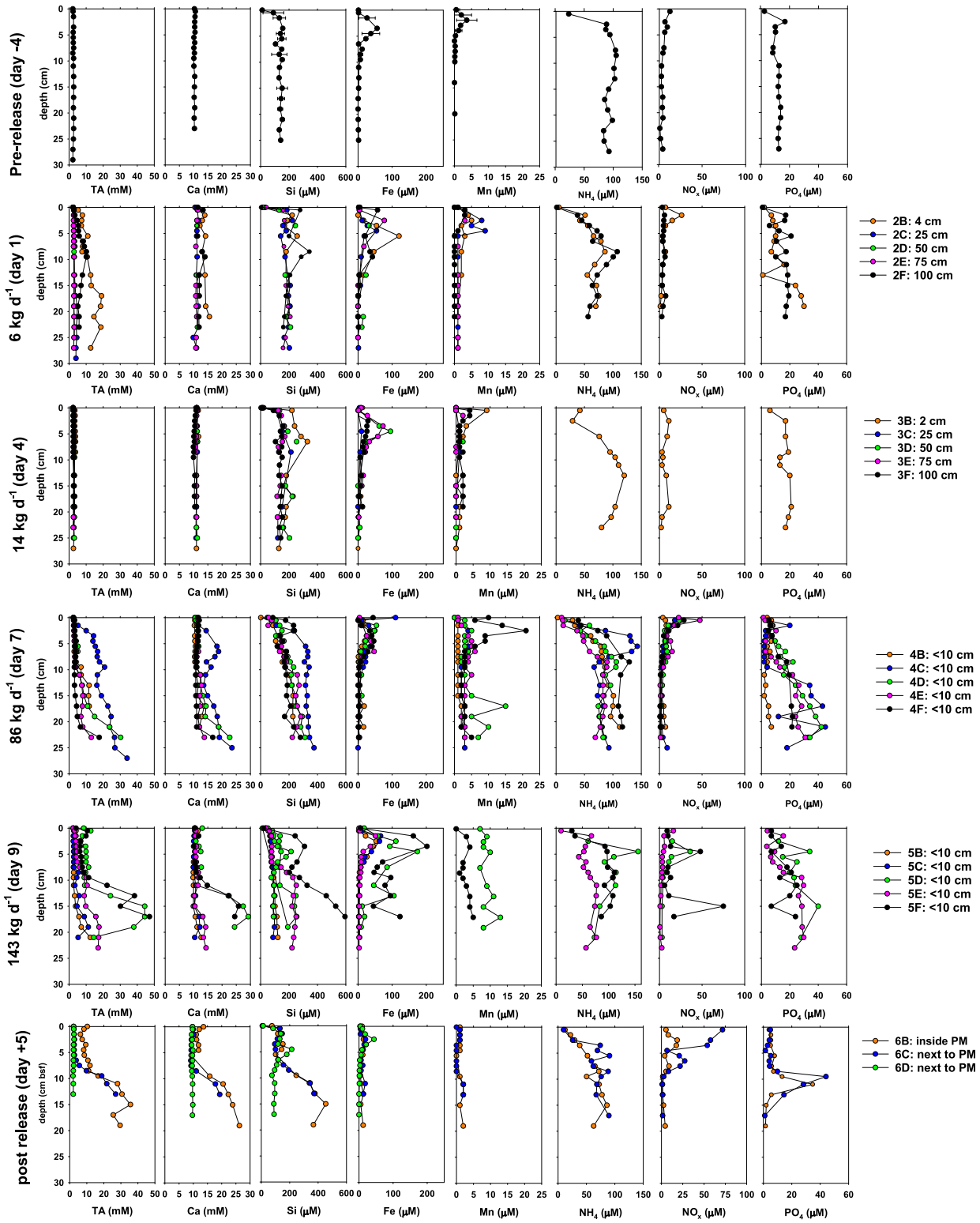

Fig. 3. Development of porewater geochemistry during the field experiment. 'Pre-release' is the average of 4 cores with standard deviations; pre-release sediments were collected 25 m SW of release site. PM = pockmark; pockmarks formed at bubble release sites and were still visible after the injection had stopped.

reducible oxides, and some with magnetite (2–9%), but most of the sedimentary iron (42–80%) was not extracted by leaching. The amount of Si mobilized was minimal (<1%), but some Si was leached during the 1st, 3rd and 4th extraction steps (carbonate-bound, reducible oxides and magnetite). In total 750–1150 µmol g^{-1} Ca, 1–7 µmol g^{-1} Mn, 250–740 µmol g^{-1} Mg, 50–190 µmol g^{-1} Fe and 10–70 µmol g^{-1} Si were leached from the sediment in all extraction steps combined, with more Fe, Mn and Si leached from sediment from below 200 cm.

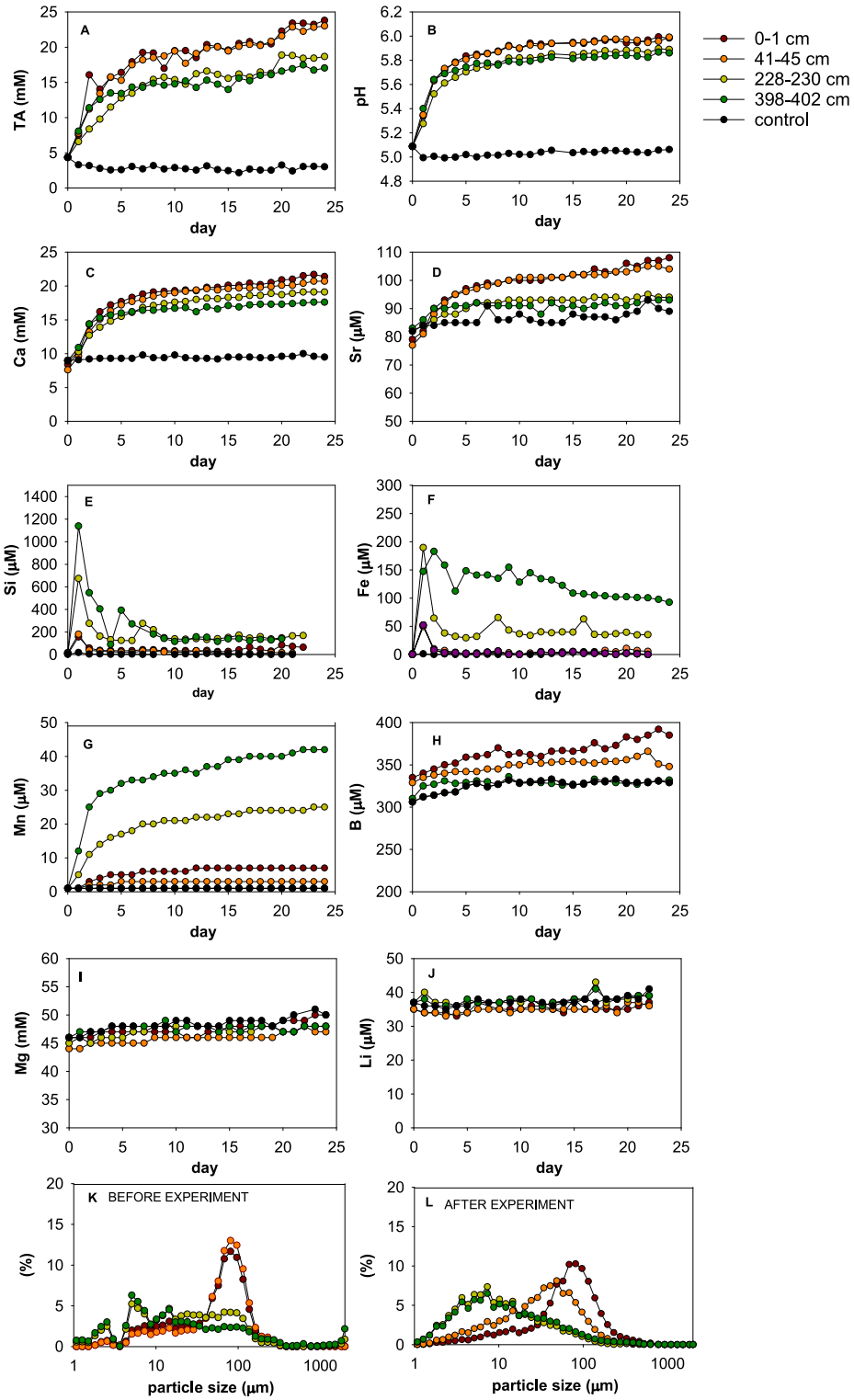

Fig. 4. Changes in TA, pH and concentrations of the elements Ca, Sr, Si, Fe, Mn, B, Mg and Li released from the sediments in the batch laboratory experiments performed with sediments from different depth intervals and changes in grain size in the sediments before and after the experiment. Results in A-J are averages of duplicate incubations.

3.5. *Modelling of the CO_2 release field experiment*

A 1-D transport-reaction model was applied to gain insights into the sinks of the injected CO_2 provided by its dissolution in the porewater and subsequent neutralization by carbonate and silicate mineral dissolution. The measured porewater profiles of total alkalinity (TA), isotopic signature of the dissolved inorganic carbon ($\delta^{13}C_{DIC}$), and metal cations (Ca, Mg, Sr, Li, B) show spatial variability (Fig. 3), but can be utilised to

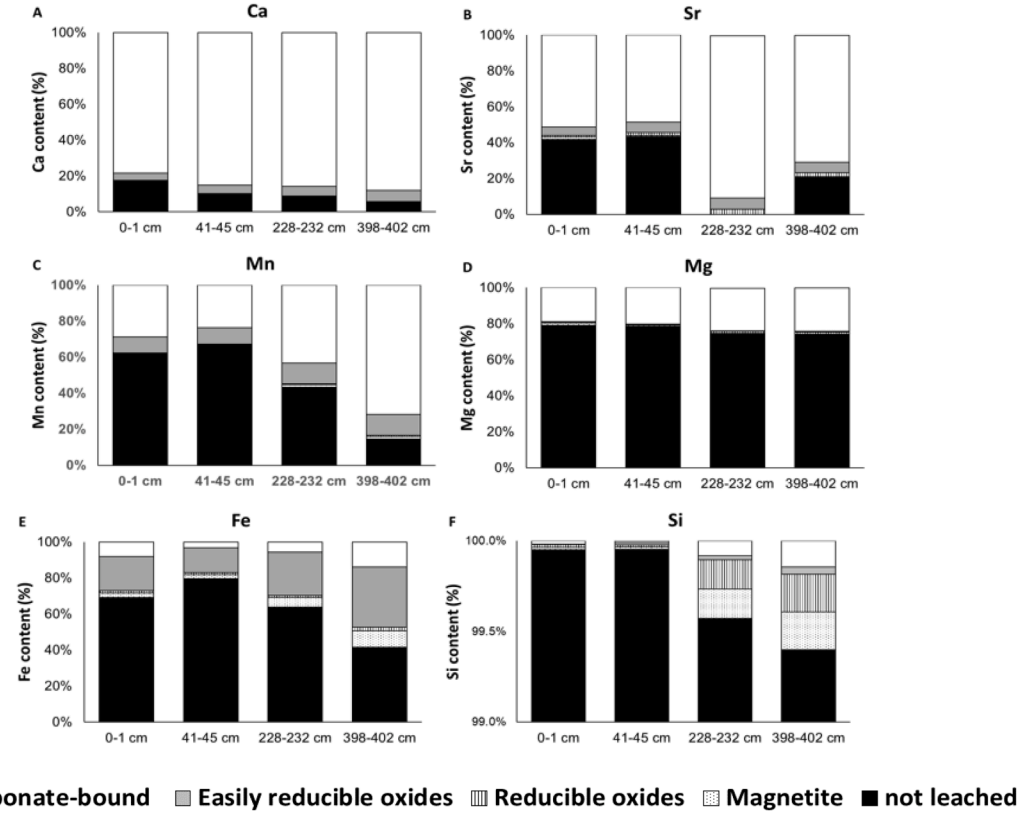

Fig. 5. Percentages of elements Ca, Sr, Mn, Mg, Fe and Si leached during the different steps of the sequential extraction from the total amount of the element contained in the sediment at different depths (measured with XRF). Note the different axis for Si.

assess reaction rates between the sediments and CO_2. As the locations of bubble streams changed over time (Flohr et al., 2021a), sediment cores were taken from close to individual bubble release spots rather than systematic transects above the injection point. Sampling on day 15, i.e., 5 days after the injection was stopped, was focused on pockmark structures that were created by the bubble release (Fig. 1, Fig. 3). These factors complicate a comparison with idealized model simulations that address the average biogeochemical behaviour above the injection point, and the model does not take into account the additional effects of irregular gas bubble release (Flohr et al., 2021a), small-scale porewater convection (Haeckel and Wallmann, 2008; O'Hara et al., 1995) and bubble irrigation (Haeckel et al., 2007).

The model runs were set up to simulate the dissolution of the injected CO_2 in a sediment depth of 200–300 cm, because seismic images showed increased reflectivity in this layer, indicative of accumulation of free gas (Roche et al., 2021). The injection overpressure of ~0.7 bar (Flohr et al., 2021a) was parameterized to drive upward advection of the porewater in the sediments above the injection point. This was realized by applying Darcy's law and an effective overburden permeability of 190 mD. Upon dissolution, the CO_2 reduces the pH of the porewater and thereby induces mineral dissolution reactions. In the model this is realized by introducing a carbonate phase and a silicate mineral with a cation stoichiometry reflecting the observed releases of Ca, Sr, Mg, Li, and B (Fig. 6). The variables DIC and TA are used as input to solve for the concentrations of the dissolved carbonate system species. The release of dissolved $Si(OH)_4$ is counteracted by the precipitation of amorphous silica (e.g., Oelkers, 2001). Hence, the numerical simulations focus on quantifying the biogeochemical processes that pose a sink for the gaseous CO_2 in the overburden sediments.

Since the measured DIC values do not reflect the in-situ concentrations and CO_2-induced mineral dissolution leads to a non-linear behaviour of the system, the stable carbon isotopic signature of the DIC was used to constrain the CO_2 dissolution rate. This was possible because the $\delta^{13}C$ value of the injected CO_2 was significantly higher (+19 ‰ V-PDB) than that of the original porewater (−2 to −4 ‰ V-PDB, Flohr et al., 2021a) and sediment carbonate (~0 ‰ V-PDB, Supplement Fig. 1). Model $\delta^{13}C_{DIC}$ values match the observed values quite well, at least until day 7, and predict a maximum value of +18.4 ‰ V-PDB (Fig. 6), a little lower than maximum measured values that are affected by loss of CO_2 during sample degassing. A DIC/TA ratio of unity demonstrates that the measured DIC is essentially identical to HCO_3^- concentrations.

Model results for porewater TA and metal cation profiles also match the observations quite well until day 7, but predicted values are lower than those measured very close to bubble sites, which were the focus of push coring after day 7. The observed high porewater concentrations are attributed to dissolution of CO_2 in the close vicinity of bubble rise paths (not shown). Initially, carbon dioxide dissolution in water is very fast, and porewaters above the injection point become CO_2-saturated within a couple of days (Supplement Fig. 2). Further CO_2 dissolution can only occur as minerals dissolve or via lateral diffusion into CO_2-poor porewaters. Both of these processes are relatively slow. pH reaches values of as low as 5 at depth (Fig. 6).

The model also provides an explanation for the unexpectedly high temperature gradients of up to ~2 °C m^{-1} observed at bubble sites (de Beer et al., 2021). Enthalpies of reactions indicate that dissolution of CO_2 can be expected to increase temperature by about 2.2 °C above background (Fig. 7), whereas dissolution of carbonate and silicate minerals contribute less than 0.1 °C to this warming effect. While the increase in temperature gradient is relatively moderate for the model scenario where CO_2 only dissolves over 200–300 cm depth (~0.5 °C m^{-1}), temperature gradients of > 5 °C m^{-1} are predicted in the upper 10 cm of the sediment column in the vicinity of bubble sites (Fig. 7).

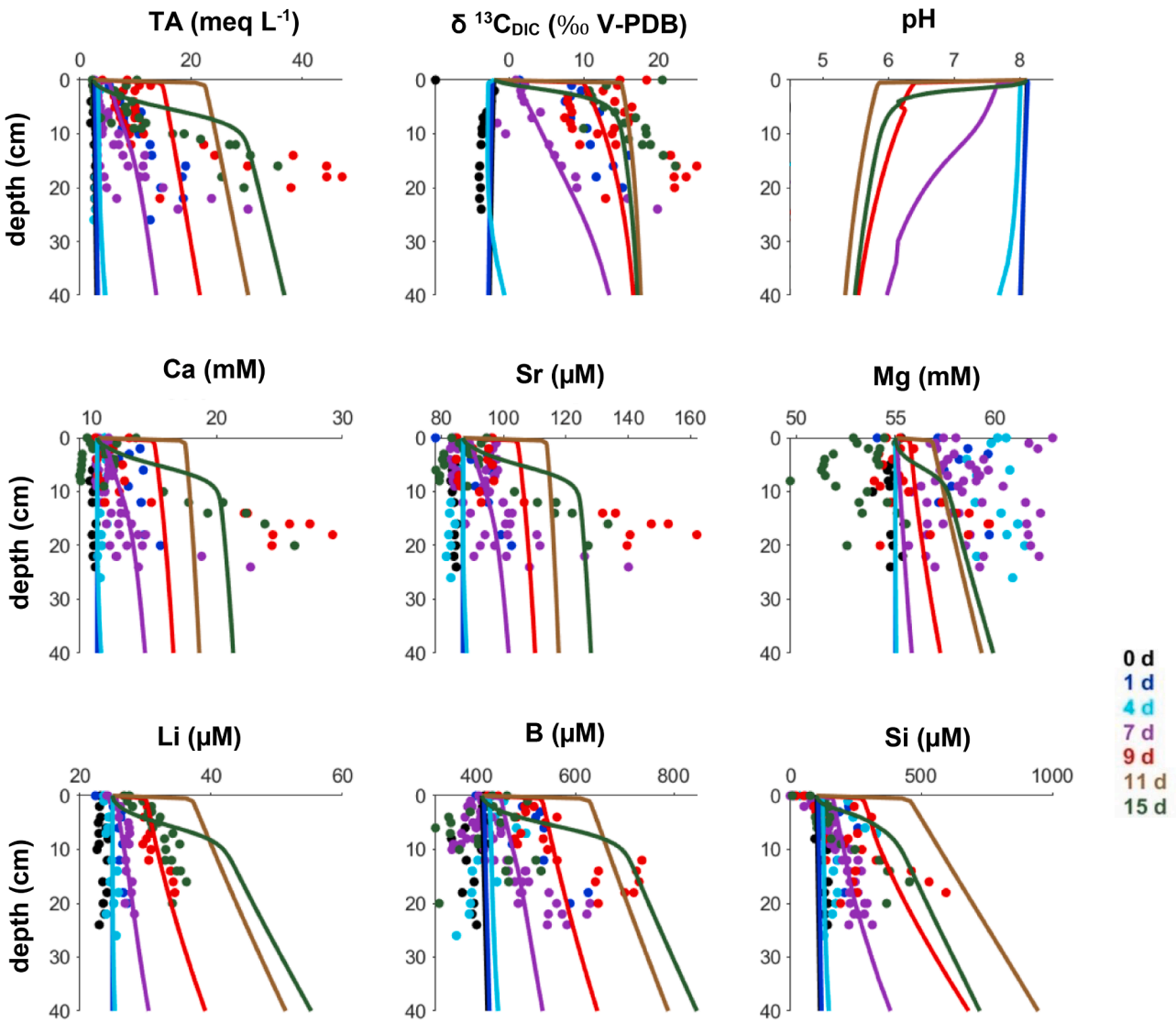

Fig. 6. Comparison of model results (lines) and measured porewater values (dots) of TA, $\delta^{13}C_{DIC}$, pH, Ca, Sr, Mg, Li, B and Si in the uppermost 40 cm. pH was not measured directly, so only model results are shown.

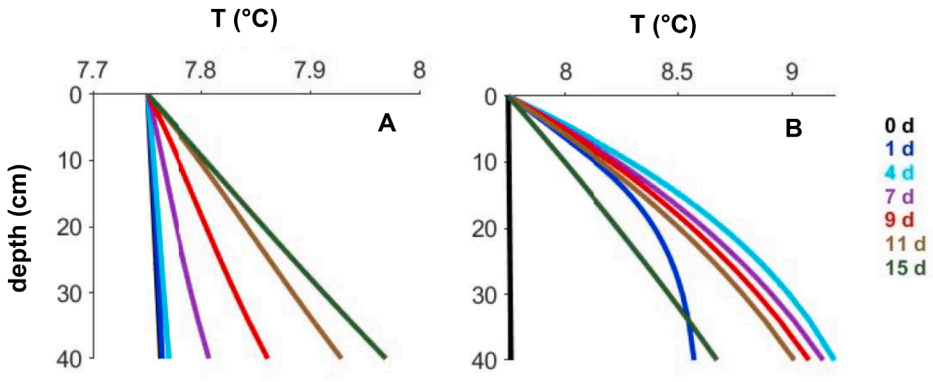

Fig. 7. Modelled temperature profiles in the uppermost 40 cm of the sediment for CO_2 dissolution occurring (A) over sediment depths of 200–300 cm, where seismic images depicted the accumulation of the injected CO_2 gas, and (B) over the entire model domain, i.e., representing dissolution in the vicinity of rising bubbles.

4. Discussion

4.1. CO_2-sediment interactions

During the in-situ CO_2 release experiment fluid transport processes and mineral-CO_2 reactions regulated the distribution of injected CO_2 and other chemical species in near-surface sediments. The CO_2 accumulated in a gas pocket at 200–300 cm depth in an area with a diameter of approximately 15 m (Roche et al., 2021). Our model showed that from here fluids migrated upwards, induced by the pressure gradient, with a velocity of ~0.3 m d^{-1}, which is 2–4 orders of magnitude higher than natural seepage rates, e.g., at methane seeps (Haeckel et al., 2004; Linke et al., 1994; Tryon et al., 1999). At the sediment surface, bubble sites were restricted to an area with a radius of 2 m (Fig. 1), and we found geochemical changes up to 1 m away from the individual bubble sites (Fig. 3).

The transport-reaction model suggests that the CO_2 injected into the sediments rapidly dissolved in the porewaters close to the CO_2 injection point, leading to a substantial drop in pH to values as low as 5 (Fig. 6). The low pH in sediment porewaters can be attributed to the injected CO_2 as the increase of porewater DIC/TA concentrations was associated with an increase of $\delta^{13}C_{DIC}$ values up to 19 ‰ V-PDB compared to the natural background of $\delta^{13}C_{DIC} = -2$ to -4 ‰ V-PDB (Flohr et al., 2021a), confirming the presence of the injected CO_2 dissolved in porewater. At such low pH values, mineral dissolution reactions are induced and the dissolved solutes are transported towards the sediment surface together with the CO_2-rich fluids as shown in previous field experiments in coastal, more sandy sediments (Lichtschlag et al., 2015). Mineral dissolution is evidenced by increased TA, Ca, Sr, Li, B, Si and Fe concentrations in porewaters (Fig. 3). The rapid, stoichiometric increases of TA, Ca, and Sr, both in the field and in the laboratory experiments (Fig. 3, Fig. 4, Supplement Fig. 3) are indicative of carbonate dissolution, which is known to be relatively fast at low pH (Plummer et al., 1978). Dissolution of carbonate minerals acts to buffer pH, but the buffer capacity of sediments is determined by a balance between the CO_2 dissolution rate, mineral reactions and upward migration of low-pH porewaters. Modelled carbonate dissolution rates were 300 mmol L^{-1} a^{-1} (Supplement Fig. 2). At this dissolution rate less than 1% of the available sedimentary carbonate content would have dissolved during the 11 days of the release experiment. This is consistent with the lack of any observable change in the inorganic carbon content of the sediments close to the bubble release sites (Supplement Fig. 1) before and after CO_2 injection. Assuming an inorganic carbon content (C_{inorg}) of approximately 1.5 wt.% in the upper 300 cm of the sediments (Fig. 2; i.e., 2250 mmol C per L of wet sediment and assuming calcite is the main carbonate mineral), at the calculated carbonate dissolution rate, it would take > 7 years to dissolve all carbonate from the sediment. Hence, for leakages scenarios similar to those tested in the field experiment, dissolution of carbonates will buffer changes in pH caused by dissolution of CO_2 in the sediment porewaters. Carbonate dissolution can also change the volume of pore space in the sediments, as shown in the laboratory experiments (Fig. 4), with a shift to finer grain sizes after exposure to CO_2-rich fluids. However, even if all carbonate was lost from the sediments, this would only marginally affect fluid migration through the sediment.

The field experiment also provided evidence for dissolution of silicate minerals under low-pH conditions, resulting in increased concentrations of Si, and to a lesser extent Mg, Li and B, in sediment porewaters. Under natural conditions silicate dissolution reactions are usually slower than carbonate reactions (e.g., Brantley et al., 2008). For example, mobilization of Si from predominately siliciclastic aquifer sediments has been shown in laboratory experiments for CO_2 leakage conditions, but with orders of magnitudes lower mobilization rates than for Ca from carbonates (Mickler et al., 2013). In CO_2-rich sediments off Japan, that are used as natural analogues for leakage impacts from CCS sites, enhanced silicate weathering by high CO_2 porewaters was suggested to be an important process (de Beer et al., 2013). Our numerical modelling shows that during the 11 days of the experiment, the dissolution of silicates may have removed just as much CO_2 as carbonate dissolution (Table 7), due to the strong initial undersaturation in the CO_2 accumulation zone at 200–300 cm depth (Supplement Fig. 2). However, the modelling also suggests that Si was only initially strongly undersaturated, and after 20 days carbonate dissolution is predicted to overtake silicate dissolution (Supplement Fig. 5). Direct comparison between field studies and laboratory experiments can be difficult due to several-orders of magnitude discrepancy between mineral dissolution rates (Moore et al., 2012; Navarre-Sitchler et al., 2011), different sediment-fluid ratios (Mickler et al., 2013; Payán et al., 2012), and fluid flow through the sediments, as shown in our field experiment. However, the modelled Si behaviour was confirmed by the laboratory experiments, with Si (and Fe) concentrations peaking during the first day of exposure to CO_2-rich fluids. Release of Si from minerals is indicated by correlation of dissolved Si with Li, B and Fe (Supplement Fig. 3), however, correlations were less well defined than for carbonate dissolution (i.e., correlations of TA and dissolved Ca and Sr; Supplement Fig. 3). In addition, in the laboratory experiment Si is negatively correlated with TA, whereas field data show a positive correlation. While precipitation of silica on mineral surfaces is known to occur (e.g., Oelkers, 2001), this has no effect on TA. For Fe, fast initial release rates followed by re-precipitation has been reported for laboratory experiments using contaminated estuarine sediments and was attributed to reductive dissolution and precipitation reactions (Martín-Torre et al., 2016). Also, as the solubility of Fe(III) in seawater is strongly pH-dependant (Millero et al., 2009), release of Fe is likely pH-related because Fe release was only observed at lowest pH (pH= 5.4); the gradual decrease of Fe in solution could be caused by re-precipitation at slightly higher pH. Association of Si and Fe to different minerals than carbonates was confirmed by the sequential extractions, where most of the leachable Si and Fe was associated with (easily) reducible oxides (Fig. 5). Fe-release from reducible Fe-oxides is common in marine sediments, however, unfortunately the mineral the released Si is associated with, could not be further determined with our extractions. For example, for hydrothermal iron oxides sorption of Si on iron-oxides has been reported with the sorption degree depending on the Si:Fe ratio (Feely et al., 1996; Jones et al., 2015). Nevertheless, the laboratory experiments confirm that some of the Si and Fe increases measured during our field study are likely related to CO_2-mineral reactions.

The modelling shows that upon dissolution, the CO_2 reduces the pH of the porewater and thereby induces mineral dissolution reactions that buffer the previously lowered pH and potentially neutralizes some of the injected CO_2. The pH of the sediment porewaters was not measured, but in situ analyses of porewater pH from microsensor measurements in the upper 10 cm of the sediment confirm that pH values were only very occasionally lower than 5.5 (de Beer et al., 2021). To understand the ultimate fate of CO_2 migrating through the sediments above the

Table 7
Modelled reaction sinks of CO_2 during the 11 days of the experiment. Carbonate and silicate dissolution are follow-up reactions of the CO_2 dissolution, as is the CO_2 loss into bottom water. Hence, they are expressed as contributions to this process.

	Mass loss/ g m^{-2}	Total mass loss inside chimney structure*/kg	Percent of total sink
CO_2 dissolution	164.7	29.1	100%
Carbonate dissolution	3.1	0.55	1.9%
Silicate dissolution	4.6	0.82	2.8%
CO_2 loss into bottom water	0.04	0.007	0.03%

* Based on available seismic data (Roche et al., 2021), the chimney-type structure has a cylindrical shape and a diameter of 15 m.

injection point and into the water column, a mass balance for the total amount of CO_2 converted to HCO_3^-/CO_3^{2-} can be estimated by integrating the reaction rates (Supplement Fig. 2) over the sediment column and multiplying them by the area of seafloor above the gas accumulation layer imaged in the seismic data (circular structure with a diameter of approximately 15 m; Roche et al., 2021). The simulations suggest that by day 11 of the experiment about 29 kg of the injected CO_2 gas had dissolved in the porewater (i.e., ~4% of the total 675 kg CO_2 injected, Table 7). Our model results indicate that less than 5% of the dissolved CO_2 was converted to HCO_3^-/CO_3^{2-} by carbonate and silicate mineral dissolution (Table 7). The model further suggests that only a negligible amount of the dissolved CO_2 was lost by diffusion into the overlying bottom water (~0.03%). Hence the majority of the CO_2 gas was either released into the water column through up to 15 separate gas bubble streams, or was retained in the sediments as gas, with the gas loss from CO_2 channels strongly depending on the gas channel diameter (de Beer et al., 2021). Compared to other studies conducted during the same CO_2 release experiment, our estimate of total CO_2 retention in the sediment is in the lower range. The main uncertainty in our extrapolated estimate originates from uncertainty of the spatial dimensions of the seismic chimney that was used for the integration of the CO_2 dissolution rates and which was changing with time (Roche et al., 2021). However, our estimate is similar to values calculated using eddy covariance in the water column (17% CO_2 retention in sediments, Koopmans et al., 2021) as this value also includes CO_2 present in the sediment in gaseous form, e.g., as shown by Roche et al., 2021. Tracers used for estimating gas dissolution in sediments, suggest that ~35% of the total injected CO_2 dissolved in the sediment (Flohr et al., 2021a).

4.2. Environmental impact and risk assessment

One concern of an accidental release of CO_2 from an offshore CCS reservoir is the impact leaking CO_2 could have on the marine environment. It is well known that CO_2 leaking into the water column will quickly be diluted by ocean currents and mixing (Dewar et al., 2013) and the footprint of the leakage will strongly depend on the leakage rate, with smaller leaks of <150 kg d^{-1} likely having only limited impact (Vielstädte et al., 2019), whereas bigger leaks would affect larger areas (e.g., 1 Mt d^{-1} would subject a seafloor area of 49 km^2 to a pH drop of 0.1 units; Blackford et al., 2020). We have shown that in the sediments, even at low leakage rates and with a strong carbonate buffer, pH can drop to values below 6 (i.e., > 2 pH units) within days of the start of the CO_2 injection (Fig. 6). Over time, porewaters in the surface sediments also become more acidic: a drop in porewater pH was observed in in-situ pH profiles. Reduction of pH may increase the bioavailability of toxic substances (Roberts et al., 2013) that could have a negative impact on infauna (Rodriguez-Romero et al., 2014). Rapid initial mobilization of trace elements, such as As, Ba, Cd, Cu, Pb and Zn, has been reported from previous aquifer sediment-CO_2 experimental studies (e.g., Kirsch et al., 2014; Wunsch et al., 2014) and was related to release of trace elements associated with metal oxyhydroxides (Karthikeyan et al., 1997; Tokoro et al., 2010) or calcite (Ahmed et al., 2008). Mobilization of metals (e.g., Co, Cu, Zn) has also been observed from coastal sediments in polluted areas under increased CO_2 conditions (de Orte et al., 2018). However, during the 11 day-long CO_2 injection into Central North Sea sediments, release of metals in concentrations that could be harmful to the environment was not detected. A previous field experiment off the Scottish coast found that the extent of metal leaching depends on the pH distribution as well as on the metal content in the sediments (Lichtschlag et al., 2015). This agrees with our laboratory experiments, which showed that the deeper sediment horizons released more metals into the porewater than near-surface sediments (Fig. 4). For example, Mn, which was associated with carbonates (Fig. 5), was released in higher amounts from the sediments below 200 cm depth. Similarly, Fe and Si releases were mainly associated with deeper sediments. Element release patterns reflect the general abundances of these elements in the sediments (Supplement Fig. 3), which had about 3 times higher concentrations in the deeper layers than at the sediment surface (Fig. 2). Hence, increased element release might be simply a function of the amount of the elements present in the sediment (Table 6). Marieni et al. (2020) showed in similar laboratory experiments that element release rates can also be a function of grain size, as fine particles have a higher ratio of surface area to volume, leading to higher dissolution rates. Hence in our experiment, in addition to the element concentrations and mineral phases, the finer grained sediments at depth might have reacted faster with CO_2 than the coarser grained, near-surface sediments, explaining the preferential release of e.g., Mn from deeper layers.

Grain sizes and metal distribution in surface sediments in the Central North Sea can be heterogeneous, but in principle our chemical analyses of the sediments were representative of the area, with similar metal contents as in surface sediments in this area (UK Block 14/2; Fugro, 2010) and other North Sea sediments (Stevenson, 2001). From these sediments, at least during short-term exposure to low-pH porewater and as long as the buffer capacity of the sediments is not exhausted, no substantial metal release should be expected. However, as we have shown that minerals will react quickly with CO_2, for a more detailed risk assessment, the lithology and geochemical composition of the overburden down to the storage reservoir needs to be known. Another concern of CO_2 leakage into the sediments is the disruption of the organic carbon degradation processes (Rastelli et al., 2016) as at natural, high-CO_2 seep sites it has been shown that long-term exposure to CO_2 has affected bacterial and metazoan community structure in the sediments (e.g., Hassenrück et al., 2016; Molari et al., 2018), which can perturb the carbon degradation process. From the distribution of the products of organic carbon degradation and the organic carbon content and isotopic ratio (Fig. 3, Supplement Fig. 1), disruption of organic carbon cycling in the sediments was not observed during short-term leakage. This is in accordance with other findings from the same field experiment that showed that aerobic respiration was similar and sulphate reduction was only slightly reduced compared to pre-release conditions (de Beer et al., 2021). Overall, our results provide further indications that the environmental impact of a CO_2 leak will be restricted to the close vicinity of the leakage structure and the subsurface CO_2 plume (Blackford et al., 2014; Wallmann et al., 2015).

For sediments close to the sediment-water interface, a more complex behaviour of dissolved components was observed during the field experiment. For example, at the highest release rate (i.e., 143 kg d^{-1}) some solutes (e.g., TA, Ca) were close to seawater concentrations in the upper 10 cm (Fig. 3), while others (e.g., Fe) showed highest concentrations close to the sediment surface. A seawater-like geochemical signature can be explained by mixing processes at the sediment surface, such as bioirrigation (the mixing depth by burrowing organisms in this area is around 10 cm, Dale et al., 2021), bubble release leading to localized infiltration of seawater into the sediment (de Beer et al., 2021), bubble-induced porewater irrigation (Haeckel et al., 2007), or by convection cells, flushing the sediment with bottom water in areas around the bubble release sites (Haeckel and Wallmann, 2008). All of these processes would effectively reduce solute concentrations in the near-surface sediments to bottom water concentrations in this mixing zone. The observed increases of dissolved iron (Fig. 3) may be attributed to very localized and patchy reduction of pH to values as low as 6, as shown by microsensor measurements (de Beer et al., 2021), i. e., low enough to increase the solubility of iron (Millero et al., 2009).

To enable large-scale implementation of offshore CCS, it is essential that appropriate tools to detect, attribute and quantify any leakage are available. Currently, most approaches target gas bubbles or pH variations in the water column (Lichtschlag et al., 2021), but also geochemical indicators, such as TA/NH_4 and TA/SO_4 ratios and chloride-normalized cation concentrations in sediment porewaters have been suggested (Dale et al., 2021). During the field study no clear correlations between TA, NH_4 and SO_4 were observed in porewaters (Supplement Fig. 3), likely because sediments were only sampled from

the bubble sites and surface sediments. However, NH_4 and PO_4 concentrations were observed to increase by up to 30% in the near-surface sediments, and as concentrations of those solutes were similar to concentrations found at 300 cm depth (Fig. 2), this might be explained by the upward advection of porewater from deeper layers, induced by the injection overpressure resulting in an advection velocity of 0.3 m d^{-1}. As advection of fluids with different composition might have a negative impact on the benthic ecosystem (Queirós et al., 2014) and the composition of the advected porewaters will vary from site to site, a proper baseline needs to be established (Blackford et al., 2021), and the geochemistry of the sediments needs to be determined. In addition, de Beer et al. (2021) have measured a temperature increase in the sediment due to CO_2 dissolution and mineral reactions. This was confirmed by our transport reaction modelling and may also be an initial diagnostic indicator of CO_2 dissolution in sediments.

5. Conclusions

This study has demonstrated that the leakage of CO_2 from a subseafloor CCS reservoir into Central North Sea sediments will lead to changes in sediment geochemistry. Elements such as Ca, Sr, Mg, Li, B, Fe and Si will be quickly mobilized from carbonates and silicate minerals, even under short and low-rate leakage conditions. In the Central North Sea, availability of potentially toxic metals in the sediments was low, but in coastal or estuarine sediments with higher metal contents, mobilization of more toxic metals could occur. Laboratory batch experiments were found to be useful for assessing the stoichiometric release of cations, however, results from the field study experiment have shown that in reality fluid flow through sediments will be more complex. Especially at the sediment surface different mixing processes can occur that impact the composition of dissolved components and might affect metal release into seawater. The spatial footprint of the geochemical leakage signature was restricted to less than 1 m from the leakage structure, and hence even at the substantial drop of pH to values of 5, at least for short, low-rate leakage in the North Sea there is no larger-scale impact on the benthic environment. Knowledge of the geophysical and geochemical properties of the sediments, such as grain size, metal content, mineral phases and fluid composition, are key factors when assessing the potential risk for the marine environment. Our numerical modelling confirmed that the temperature increase in the sediment upon CO_2 dissolution and precursors fluids might be useful as leakage indicator and could in the future form part of the monitoring strategy.

Declaration of Competing Interest

The authors declare that they have no known competing financial interests or personal relationships that could have appeared to influence the work reported in this paper.

Acknowledgment

The authors would like to thank the captains and crews and RV *Poseidon* and RRV *James Cook* and of the remote-operated vehicle ISIS for their excellent support during the research expeditions. We thank James Strong for the very helpful discussions about the core location map. The British Ocean Sediment Core Research Facility (BOSCORF) is thanked for using their facilities. This research received funding from the European Union's Horizon 2020 research and innovation programme under grant agreement No. 654462 (STEMM-CCS) and by the Natural Environment Research Council NERC Highlight Topic CHIMNEY (NE/N016130/1). We thank the editors and reviewers for their positive and constructive comments.

Supplementary materials

Supplementary material associated with this article can be found, in the online version, at doi:10.1016/j.ijggc.2021.103352.

References

Ahmed, I.A., Crout, N.M., Young, S.D., 2008. Kinetics of Cd sorption, desorption and fixation by calcite: a long-term radiotracer study. Geochim. Cosmochim. Acta 72, 1498–1512.
Aiuppa, A., Hall-Spencer, J., Milazzo, M., Turco, G., Caliro, S., Di Napoli, R., 2021. Volcanic CO_2 seep geochemistry and use in understanding ocean acidification. Biogeochemistry 152, 93–115.
Ardelan, M.V., Steinnes, E., Lierhagen, S., Linde, S.O., 2009. Effects of experimental CO_2 leakage on solubility and transport of seven trace metals in seawater and sediment. Sci. Total Environ. 407, 6255–6266.
Arndt, S., Jørgensen, B.B., LaRowe, D.E., Middelburg, J., Pancost, R., Regnier, P., 2013. Quantifying the degradation of organic matter in marine sediments: a review and synthesis. Earth-Sci. Rev. 123, 53–86.
Berner, R.A., 1980. Early diagenesis: a theoretical approach. Princeton University Press.
Blackford, J., Alendal, G., Avlesen, H., Brereton, A., Cazenave, P.W., Chen, B., Dewar, M., Holt, J., Phelps, J., 2020. Impact and detectability of hypothetical CCS offshore seep scenarios as an aid to storage assurance and risk assessment. Int. J. Greenhouse Gas Control 95, 102949.
Blackford, J., Romanek, K., Huevenne, V., Strong, J., Durden, J., Lichtschlag, A., Connelly, D., 2021. Repurposing oceanographic data to provide a robust marine environmental characterisation to support offshore geological CO_2 storage monitoring. Int. J. Greenhouse Gas Control.
Blackford, J., Stahl, H., Bull, J.M., Bergès, B.J., Cevatoglu, M., Lichtschlag, A., Connelly, D., James, R.H., Kita, J., Long, D, 2014. Detection and impacts of leakage from sub-seafloor deep geological carbon dioxide storage. Nat. Clim. Chang. 4, 1011–1016.
Boudreau, B.P., 1997. Diagenetic Models and Their Implementation. Springer, Berlin.
Brantley, S.L., Kubicki, J.D., White, A.F., 2008. Kinetics of Water-Rock Interaction. Springer.
Cevatoglu, M., Bull, J.M., Vardy, M.E., Gernon, T.M., Wright, I.C., Long, D, 2015. Gas migration pathways, controlling mechanisms and changes in sediment acoustic properties observed in a controlled sub-seabed CO_2 release experiment. Int. J. Greenhouse Gas Control 38, 26–43.
Cotton, A., Gray, L., Maas, W., 2017. Learnings from the Shell Peterhead CCS project front end engineering design. Energy Procedia 114, 5663–5670.
Croudace, I.W., Rindby, A., Rothwell, R.G., 2006. ITRAX: Description and Evaluation of a New Multi-Function X-ray Core Scanner, 267. Geological Society, London, pp. 51–63. Special Publications.
Dale, A., Sommer, S., Lichtschlag, A., Koopmans, D., Haeckel, M., Kossel, E., Deusner, C., Linke, P., Scholten, J., Wallmann, K., Erik, M.v., Gros, J., Scholz, F., Schmidt, M., 2021. Defining a biogeochemical baseline for sediments at Carbon Capture and Storage (CCS) sites: an example from the North Sea (Goldeneye). Int. J. Greenhouse Gas Control 106, 103265.
de Beer, D., Haeckel, M., Neumann, J., Wegener, G., Inagaki, F., Boetius, A., 2013. Saturated CO_2 inhibits microbial processes in CO_2-vented deep-sea sediments. Biogeosciences 10, 5639–5649.
de Beer, D., Lichtschlag, A., Flohr, A., van Erk, M.R., Ahmerkamp, S., Holtappels, M., Haeckel, M., Strong, J., 2021. Sediment acidification and temperature increase in an artificial CO_2 vent. Int. J. Greenhouse Gas Control 105, 103244.
de Orte, M.R., Bonnail, E., Sarmiento, A.M., Bautista-Chamizo, E., Basallote, M.D., Riba, I., DelValls, Á., Nieto, J.M., 2018. Metal fractionation in marine sediments acidified by enrichment of CO_2: a risk assessment. Mar. Pollut. Bull. 131, 611–619.
Dean, M., Tucker, O., 2017. A risk-based framework for Measurement, Monitoring and Verification (MMV) of the Goldeneye storage complex for the Peterhead CCS project. UK. Int. J. Greenhouse Gas Control 61, 1–15.
Dewar, M., Wei, W., McNeil, D., Chen, B., 2013. Small-scale modelling of the physiochemical impacts of CO_2 leaked from sub-seabed reservoirs or pipelines within the North Sea and surrounding waters. Mar. Pollut. Bull. 73, 504–515.
Energy, 2016. Progressing Development of the UK's Strategic Carbon Dioxide Storage resource. A Summary of Results from the Strategic UK CO_2. Pale Blue Dot Energy.
Fabricius, K.E., Langdon, C., Uthicke, S., Humphrey, C., Noonan, S., De'ath, G., Okazaki, R., Muehllehner, N., Glas, M.S., Lough, J.M., 2011. Losers and winners in coral reefs acclimatized to elevated carbon dioxide concentrations. Nat. Clim. Chang. 1, 165–169.
Feely, R., Baker, E., Marumo, K., Urabe, T., Ishibashi, J., Gendron, J., Lebon, G., Okamura, K., 1996. Hydrothermal plume particles and dissolved phosphate over the superfast-spreading southern East Pacific Rise. Geochim. Cosmochim. Acta 60, 2297–2323.
Flohr, A., Matter, J.M., James, R.H., Saw, K., Brown, R., Gros, J., Flude, S., Day, C., Peel, K., Connelly, D., Pearce, C., Strong, J.A., Lichtschlag, A., Hillegonds, D.J., Ballentine, C.J., Tyne, R.L., 2021a. Utility of natural and artificial geochemical tracers for leakage monitoring and quantification during an offshore controlled CO_2 release experiment. Int. J. Greenhouse Gas Control.
Flohr, A., Schaap, A., Achterberg, E.P., Alendal, G., Arundell, M., Berndt, C., Blackford, J., Böttner, C., Borisov, S.M., Brown, R., Bull, J.M., Carter, L., Chen, B., Dale, A.W., de Beer, D., Dean, M., Deusner, C., Dewar, M., Durden, J.M., Elsen, S., Esposito, M., Faggetter, M., Fischer, J., Gana, A., Gros, J., Haeckel, M., Hanz, R., Holtappels, M., Hosking, B., Huvenne, V.A.I., James, R.H., Koopmans, D., Kossel, E., Leighton, T.G., Li, J., Lichtschlag, A., Linke, P., Loucaides, S., Martínez-Cabanas, M., Matter, J.M., Mesher, T., Monk, S., Mowlem, M., Oleynik, A., Papadimitriou, S., Paxton, D., Pearce, C.R., Peel, K., Roche, B., Ruhl, H.A., Saleem, U., Sands, C., Saw, K., Schmidt, M., Sommer, S., Strong, J.A., Triest, J., Ungerböck, B., Walk, J.,

White, P., Widdicombe, S., Wilson, R.E., Wright, H., Wyatt, J., Connelly, D, 2021b. Towards improved monitoring of offshore carbon storage: a real-world field experiment detecting a controlled sub-seafloor CO_2 release. Int. J. Greenhouse Gas Control 106, 103237.

Fugro (2010) Envionmetnal Survey, UKCS Block 14/29 & 20/4 Goldeneye Field.

Gattuso, J.-.P., Magnan, A., Billé, R., Cheung, W.W., Howes, E.L., Joos, F., Allemand, D., Bopp, L., Cooley, S.R., Eakin, C.M., 2015. Contrasting futures for ocean and society from different anthropogenic CO_2 emissions scenarios. Science 349.

Haeckel, M., Boudreau, B.P., Wallmann, K., 2007. Bubble-induced porewater mixing: a 3-D model for deep porewater irrigation. Geochim. Cosmochim. Acta 71, 5135–5154.

Haeckel, M., Suess, E., Wallmann, K., Rickert, D, 2004. Rising methane gas bubbles form massive hydrate layers at the seafloor. Geochim. Cosmochim. Acta 68, 4335–4345.

Haeckel, M., Wallmann, K., 2008. Indications for convective flow induced by focussed fluid venting at bacterial mats. Geochim. Cosmochim. Acta A339–A405.

Hall-Spencer, J.M., Rodolfo-Metalpa, R., Martin, S., Ransome, E., Fine, M., Turner, S.M., Rowley, S.J., Tedesco, D., Buia, M.-.C., 2008. Volcanic carbon dioxide vents show ecosystem effects of ocean acidification. Nature 454, 96–99.

Hassenrück, C., Fink, A., Lichtschlag, A., Tegetmeyer, H.E., de Beer, D., Ramette, A., 2016. Quantification of the effects of ocean acidification on sediment microbial communities in the environment: the importance of ecosystem approaches. FEMS Microbiol. Ecol. 92, fiw027.

IEA, 2015. Energy Technology Perspectives. Paris, France, p. 406.

IPCC (2005) Special Report on Carbon Dioxide Capture and Storage. Prepared by Working Group III of the Intergovernmental Panel on Climate Change in: Metz, B., O. Davidson, H. C. de Coninck, M. Loos, and L. A. Meyer (Ed.), IPCC, Cambridge University Press, The Edinburgh Building Shaftesbury Road, Cambridge, England.

Jones, C., Nomosatryo, S., Crowe, S.A., Bjerrum, C.J., Canfield, D.E., 2015. Iron oxides, divalent cations, silica, and the early earth phosphorus crisis. Geology 43, 135–138.

Karthikeyan, K., Elliott, H.A., Cannon, F.S., 1997. Adsorption and coprecipitation of copper with the hydrous oxides of iron and aluminum. Environ. Sci. Technol. 31, 2721–2725.

Kim, H., Kim, Y.H., Kang, S.-.G., Park, Y.-.G., 2016. Development of environmental impact monitoring protocol for offshore carbon capture and storage (CCS): a biological perspective. Environ. Impact Assess. Rev. 57, 139–150.

Kirsch, K., Navarre-Sitchler, A.K., Wunsch, A., McCray, J.E., 2014. Metal release from sandstones under experimentally and numerically simulated CO_2 leakage conditions. Environ. Sci. Technol. 48, 1436–1442.

Koopmans, D., Meyer, V., Schaap, A., Dewar, M., Färber, P., Long, M.H., Connelly, D., Holtappels, M., 2021. Detection and quantification of a release of carbon dioxide gas from the seafloor using pH eddy covariance and measurements of plume advection. Int. J. Greenh. Gas Control 48.

Kossel, E., Bigalke, N.K., Pinero, E., Haeckel, M., 2013. The SUGAR Toolbox: a Library of Numerical Algorithms and Data For Modelling of Gas Hydrate Systems and Marine Environments. PANGAEA, Bremerhaven.

Lichtschlag, A., James, R.H., Stahl, H., Connelly, D, 2015. Effect of a controlled sub-seabed release of CO_2 on the biogeochemistry of shallow marine sediments, their pore waters, and the overlying water column. Int. J. Greenhouse Gas Control 38, 80–92.

Lichtschlag, A., Pearce, R.C., Suominen, M., Blackford, J., Borisov, S.M., Bull, J.M., deBeer, D., Dean, M., Flohr, A., Esposito, M., Gros, J., Haeckel, M., Huvenne, V.A.I., James, R.H., Koopmans, D., Linke, P., Mowlem, M., Omar, A.M., Schaap, A., Schmidt, M., Sommer, S., Strong, J., Connelly, D.P, 2021. Suitability analysis and revised strategies for marine environmental carbon capture and storage (CCS) monitoring. Int. J. Greenhouse Gas Control.

Linke, P., Suess, E., Torres, M., Martens, V., Rugh, W., Ziebis, W., Kulm, L., 1994. In situ measurement of fluid flow from cold seeps at active continental margins. Deep Sea Res. Part I 41, 721–739.

Marieni, C., Matter, J.M., Teagle, D.A., 2020. Experimental study on mafic rock dissolution rates within CO_2-seawater-rock systems. Geochim. Cosmochim. Acta 272, 259–275.

Martín-Torre, M.C., Ruiz, G., Galán, B., Viguri, J.R., 2016. CO_2 seawater acidification by CCS-simulated leakage: kinetic modelling of Zn, Pb, Cd, Ni, Cr, Cu and As release from contaminated estuarine sediment using pH-static leaching tests. Int. J. Greenhouse Gas Control 54, 185–199.

Martins, M., Carreiro-Silva, M., Martins, G.M., e Ramos, J.B., Viveiros, F., Couto, R.P., Parra, H., Monteiro, J., Gallo, F., Silva, C., 2021. Ervilia castanea (Mollusca, Bivalvia) populations adversely affected at CO_2 seeps in the North Atlantic. Sci. Total Environ. 754, 142044.

Mickler, P.J., Yang, C., Scanlon, B.R., Reedy, R., Lu, J., 2013. Potential impacts of CO_2 leakage on groundwater chemistry from laboratory batch experiments and field push–pull tests. Environ. Sci. Technol. 47, 10694–10702.

Middelburg, J.J., 2011. Chemoautotrophy in the ocean. Geophys. Res. Lett. 38.

Millero, F.J., Woosley, R., DiTrolio, B., Waters, J., 2009. Effect of ocean acidification on the speciation of metals in seawater. Oceanography 22, 72–85.

Molari, M., Guilini, K., Lott, C., Weber, M., de Beer, D., Meyer, S., Ramette, A., Wegener, G., Wenzhöfer, F., Martin, D, 2018. CO_2 leakage alters biogeochemical and ecological functions of submarine sands. Sci. Adv. 4, eaao2040.

Moore, J., Lichtner, P.C., White, A.F., Brantley, S.L., 2012. Using a reactive transport model to elucidate differences between laboratory and field dissolution rates in regolith. Geochim. Cosmochim. Acta 93, 235–261.

Nagelkerken, I., Connell, S.D., 2015. Global alteration of ocean ecosystem functioning due to increasing human CO_2 emissions. Proc. Natl. Acad. Sci. 112, 13272–13277.

Navarre-Sitchler, A., Steefel, C.I., Sak, P.B., Brantley, S.L., 2011. A reactive-transport model for weathering rind formation on basalt. Geochim. Cosmochim. Acta 75, 7644–7667.

O'Hara, S.C.M., Dando, P.R., Schuster, U., Bennis, A., Boyle, J.D., Chui, F.T.W., Hatherell, T.V.J., Niven, S.J., Taylor, L.J, 1995. Gas seep induced interstitial water circulation: observations and environmental implications. Cont. Shelf Res. 15, 931–948.

Oelkers, E.H., 2001. General kinetic description of multioxide silicate mineral and glass dissolution. Geochim. Cosmochim. Acta 65, 3703–3719.

Ostertag-Henning, C., Risse, A., Thomas, B., Rosenbauer, R., Rochelle, C., Purser, G., Kilpatrick, J.Rosenqvist, Yardley, B., Karamalidis, A., Griffith, C., Hedges, S., Dilmore, R., Goodman, A., Black, J., Haese, R., Deusner, C., Bigalke, N., Haeckel, M., Fischer, S., Liebscher, A., Icenhower, J.P., Daval, D., Saldi, G.D., Knauss, K.G., Schmidt, M., Mito, S., Sorai, M., Truche, L., 2014. GaMin'11 – an International Inter-laboratory comparison for Geochemical CO_2 - Saline Fluid - Mineral Interaction Experiments. Energy Procedia 63, 5538–5543.

Payán, M.C., Verbinnen, B., Galan, B., Coz, A., Vandecasteele, C., Viguri, J.R., 2012. Potential influence of CO_2 release from a carbon capture storage site on release of trace metals from marine sediment. Environ. Pollut. 162, 29–39.

Plummer, L., Wigley, T., Parkhurst, D, 1978. The kinetics of calcite dissolution in CO_2-water systems at 5 degrees to 60 °C and 0.0 to 1.0 atm CO_2. Am. J. Sci. 278, 179–216.

Poulton, S.W., Canfield, D.E., 2005. Development of a sequential extraction procedure for iron: implications for iron partitioning in continentally derived particulates. Chem. Geol. 214, 209–221.

Queirós, A.M., Norling, K., Amaro, T., Nunes, J., Cummings, D., Yakushev, E., Sorensen, K., Harris, C., Woodward, M. and Danovaro, R. (2014) Potential impact of CCS leakage on marine communities. EU ECO2 Project. Deliverable 4.1. doi:10.3289/ECO2_D4.1.

Rastelli, E., Corinaldesi, C., Dell'Anno, A., Amaro, T., Greco, S., Martire, M.L., Carugati, L., Queirós, A.M., Widdicombe, S., Danovaro, R., 2016. CO_2 leakage from carbon dioxide capture and storage (CCS) systems affects organic matter cycling in surface marine sediments. Mar. Environ. Res. 122, 158–168.

Roberts, D.A., Birchenough, S.N., Lewis, C., Sanders, M.B., Bolam, T., Sheahan, D, 2013. Ocean acidification increases the toxicity of contaminated sediments. Glob. Chang. Biol. 19, 340–351.

Roche, B., Bull, J., White, P., Li, J., Leighton, T., 2021. Time-lapse imaging of CO_2 migration within near-surface sediments during a controlled sub-seabed release experiment. Int. J. Greenhouse Gas Control.

Rodriguez-Romero, A., Basallote, M.D., Manoela, R., DelValls, T.Á., Riba, I., Blasco, J., 2014. Simulation of CO_2 leakages during injection and storage in sub-seabed geological formations: metal mobilization and biota effects. Environ. Int. 68, 105–117.

Smith, J.N., De'ath, G., Richter, C., Cornils, A., Hall-Spencer, J.M., Fabricius, K.E., 2016. Ocean acidification reduces demersal zooplankton that reside in tropical coral reefs. Nat. Clim. Chang 6, 1124–1129.

Stevenson, A.G., 2001. Metal concentrations in marine sediments around Scotland: a baseline for environmental studies. Cont. Shelf Res. 21, 879–897.

Stumm, W., Morgan, J.J., 1996. Aquatic Chemistry. John Wiley & Sons, New York.

Tokoro, C., Yatsugi, Y., Koga, H., Owada, S., 2010. Sorption mechanisms of arsenate during coprecipitation with ferrihydrite in aqueous solution. Environ. Sci. Technol. 44, 638–643.

Tryon, M.D., Brown, K.M., Torres, M.E., Tréhu, A.M., McManus, J., Collier, R.W., 1999. Measurements of transience and downward fluid flow near episodic methane gas vents, Hydrate Ridge, Cascadia. Geology 27, 1075–1078.

Vangkilke-Pederson, T. (2009) GeoCapacity Project. D 16 WP2 Report: storage Capacity Deliverable report for the EU GeoCapacity Project.

Vielstädte, L., Karstens, J., Haeckel, M., Schmidt, M., Linke, P., Reimann, S., Liebetrau, V., McGinnis, D.F., Wallmann, K., 2015. Quantification of methane emissions at abandoned gas wells in the Central North Sea. Mar Pet Geol 68, 848–860.

Vielstädte, L., Linke, P., Schmidt, M., Sommer, S., Haeckel, M., Braack, M., Wallmann, K., 2019. Footprint and detectability of a well leaking CO_2 in the Central North Sea: implications from a field experiment and numerical modelling. Int. J. Greenhouse Gas Control 84, 190–203.

Wallmann, K., Haeckel, M., Linke, P., Haffert, L., Schmidt, M., Buenz, S., James, R., Hauton, C., Tsimplis, M., Widdicombe, S., Blackford, J., Queiros, A.M., Connelly, D., Lichtschlag, A., Dewar, M., Chen, B., Baumberger, T., Beaubin, S., Vercelli, S., Proelss, A., Wildenborg, T., Mikunda, T., Nepveu, M., Maynard, C., Finnerty, S., Flach, T., Ahmed, N., Ulfsnes, A., Brooks, L., T., M. and M., P. (2015) Best practice guidance for environmental risk assessment for offshore CO2 geological storage. EU ECO2 Project. D14.1. doi:10.3289/ECO2_D14.1.53.

Werner, R.A., Brand, W.A., 2001. Referencing strategies and techniques in stable isotope ratio analysis. Rapid Commun. Mass Spectrom. 15, 501–519.

Wunsch, A., Navarre-Sitchler, A.K., Moore, J., McCray, J.E., 2014. Metal release from limestones at high partial-pressures of CO_2. Chem. Geol. 363, 40–55.

Zander, T., Haeckel, M., Klaucke, I., Bialas, J., Klaeschen, D., Papenberg, C., Pape, T., Berndt, C., Bohrmann, G., 2020. New insights into geology and geochemistry of the Kerch seep area in the Black Sea. Mar Pet Geol 113, 104162.